The Journal of Chemical Physics

Exotic electronic structures of $Sm_xCe_{3-x}O_y$ (x = 0-3; y = 2-4) clusters and the effect of high neutral density of low-lying states on photodetachment transition intensities

Cite as: J. Chem. Phys. **149**, 054305 (2018); https://doi.org/10.1063/1.5043490
Submitted: 09 June 2018 . Accepted: 19 July 2018 . Published Online: 07 August 2018

Josey E. Topolski, Jared O. Kafader, Vicmarie Marrero-Colon, Srinivasan S. Iyengar, Hrant P. Hratchian, and Caroline Chick Jarrold

Exotic electronic structures of $Sm_xCe_{3-x}O_y$ (x = 0-3; y = 2-4) clusters and the effect of high neutral density of low-lying states on photodetachment transition intensities

Josey E. Topolski,[1] Jared O. Kafader,[1,a)] Vicmarie Marrero-Colon,[1,b)] Srinivasan S. Iyengar,[1] Hrant P. Hratchian,[2] and Caroline Chick Jarrold[1,c)]
[1]*Department of Chemistry, Indiana University, 800 East Kirkwood Ave., Bloomington, Indiana 47405, USA*
[2]*Department of Chemistry and Chemical Biology, University of California, Merced, 5200 North Lake Road, Merced, California 95343, USA*

(Received 9 June 2018; accepted 19 July 2018; published online 7 August 2018)

Lanthanide (*Ln*) oxide clusters have complex electronic structures arising from the partially occupied *Ln* 4*f* subshell. New anion photoelectron (PE) spectra of $Sm_xCe_{3-x}O_y^-$ (x = 0–3; *y* = 2–4) along with supporting results of density functional theory (DFT) calculations suggest interesting *x* and *y*-dependent Sm 4*f* subshell occupancy with implications for Sm-doped ionic conductivity of ceria, as well as the overall electronic structure of the heterometallic oxides. Specifically, the Sm centers in the heterometallic species have higher 4*f* subshell occupancy than the homonuclear $Sm_3O_y^-/Sm_3O_y$ clusters. The higher 4*f* subshell occupancy both weakens Sm—O bonds and destabilizes the 4*f* subshell relative to the predominantly O 2*p* bonding orbitals in the clusters. Parallels between the electronic structures of these small cluster systems with bulk oxides are explored. In addition, unusual changes in the excited state transition intensities, similar to those observed previously in the PE spectra of Sm_2O^- and $Sm_2O_2^-$ [J. O. Kafader *et al.*, J. Chem. Phys. **146**, 194310 (2017)], are also observed in the relative intensities of electronic transitions to excited neutral state bands in the PE spectra of $Sm_xCe_{3-x}O_y^-$ (*x* = 1–3; *y* = 2, 4). The new spectra suggest that the effect is enhanced with lower oxidation states and with an increasing number of Sm atoms, implying that the prevalence of electrons in the diffuse Sm 6*s*-based molecular orbitals and a more populated 4*f* subshell both contribute to this phenomenon. Finally, this work identifies challenges associated with affordable DFT calculations in treating the complex electronic structures exhibited by these systems, including the need for a more explicit treatment of strong coupling between the neutral and PE. *Published by AIP Publishing.*
https://doi.org/10.1063/1.5043490

I. INTRODUCTION

The lanthanoid (*Ln*) series of metals, which typically assume the sesquioxide stoichiometry, Ln_2O_3, are chemically similar:[1] In the sequence of metals ranging from La to Lu, each incremental increase in the nuclear charge is generally accompanied by an incremental increase in the nuclear-shielding 4*f* subshell occupancy.[2] This progression in 4*f* subshell occupancy is chemically different from the progression in ***nd*** subshell occupancy in the transition metals because of the relatively low orbital overlap associated with contracted 4*f* orbitals, making them more core-like rather than chemically bonding. Exceptions to the favored +3 oxidation state among the lanthanides include Ce and Eu. Ceria, CeO_2, is the more favored cerium oxide, though Ce can toggle between +3 and +4 oxidation states,[3] while the +2 oxidation state of Eu is favored because of the particular stability of the half-filled 4*f* subshell.

Ceria, in particular, has been investigated vigorously for catalytic applications[4–11] and as an ionically conducting solid electrolyte (O^{2-} as charge carrier) utilized in solid oxide fuel cells (SOFCs).[12–16] Of relevance to the latter, ionic conductivity can be enhanced by oxygen vacancies,[17,18] doping,[19,20] and increased surface area in nanoparticle systems.[21,22] Doped ZnO_2 and ThO_2 have been considered for use in SOFCs, but operating temperatures of over 1000 °C[23,24] have made them impractical for large scale production. The ionic conductivity of ceria doped with samarium, in particular, has proven to be a promising alternative to doped ZnO_2 and ThO_2, with reduced operating temperatures between 400 and 600 °C.[25–27] Oxygen vacancies in the fluorite CeO_2 crystal structure introduced from trivalent dopants, such as Sm, account for the increase in ionic conductivity.[28–31] The optimal dopant concentration of Sm has not been well established, though it is in the range of *x* = 0.10–0.20 for $Ce_{1-x}Sm_xO_2$ stoichiometry.[32]

Because bonding in metal oxide systems is localized, cluster models[33,34] of bulk metal oxides can give insight into the local metal-metal interactions in these mixed metal

[a)]Current address: Department of Chemistry, Northwestern University, 2145 Sheridan Road, Evanston, IL 60208, USA.
[b)]Current address: Universidad Metropolitana, San Juan 00926, Puerto Rico, USA.
[c)]Author to whom correspondence should be addressed: cjarrold@indiana.edu

systems that can be complementary to results of studies on bulk systems,[35–40] particularly in efforts to characterize the local features such as defect and dopant sites. In our research program, we have focused on metal oxides in lower-than-traditional oxidation states (suboxides) as models for oxygen vacancies on defective metal oxide surfaces, which are implicated in some catalytic processes.[11,41–43] An important feature of heteronuclear transition metal suboxide cluster properties is that the asymmetry of oxidation states is governed more by disparate metal oxophilicity than by disparate valency. As a particularly dramatic example, the $MoWO_3^-$ cluster anion structure can be described as the Mo^- atomic anion electrostatically bound to the fully oxidized WO_3 molecule (both Mo and W being Group 6 transition metals), while the structure of the bulk stoichiometric $MoWO_6^-$ cluster has both metal centers in the +5.5 oxidation state or +6 for the neutral cluster.[44] The methods we have used to determine the electronic and molecular structures of these clusters include anion photoelectron (PE) spectroscopy in combination with calculations, which have been shown to be particularly well suited to the study of metal oxides and complexes by ourselves and others.[45–70]

As an extension on a recent study on small $Sm_xCe_{2-x}O_y^-$ (x = 0–2; y = 1, 2) clusters, in this report, we present and analyze the PE spectra and of a systematic series of homo- and heteronuclear trimetallic cerium/samarium oxide clusters $Sm_xCe_{3-x}O_y^-$ (x = 0–3) in a range of suboxide states (y = 2–4). The atomic numbers of cerium and samarium are 58 and 62, respectively. The CeO and SmO diatomic molecular electronic structures following the 4*f* subshell occupancy trend along the lanthanoid series noted above: In their ground electronic states, Ce has a 4*f* subshell occupancy and Sm has a $4f^5$ subshell occupancy in their respective *Ln*O diatomic molecules.[71] The analyses of the $Sm_xCe_{3-x}O_y^-$ PE spectra, supported by density functional theory (DFT) calculations, indicate that the Sm 4*f* subshell occupancy is higher than $4f^5$ in both mixed and the most reduced homonuclear species, which results in a weaker Sm–O bond compared to Ce–O.

The electronic structures of the trimetallic suboxide clusters in this study are compared and contrasted with species in comparable oxidation states, CeO^- and $Ce_xO_y^-$ clusters[72,73] along with $Sm_2O_y^-$ and $SmCeO_y^-$ (y = 1–2) clusters,[74] and SmO^-, which was recently studied using slow electron velocity map imaging spectroscopy by Neumark and co-workers.[75] We also present results of density functional theory calculations, which have proven to be qualitatively informative, though with these larger systems, we also identify critical shortcomings of this inexpensive computation approach to exceptionally complex electronic structure calculations.

While the PE spectra of the most oxidized species in this series of clusters, $Sm_xCe_{3-x}O_4^-$, are fairly simple, reflecting the high symmetry of the structures formed with particular oxidation state, the spectra of the less oxidized species are more complex. This effect is anticipated because the less oxidized clusters necessarily have more electrons populating the plethora of close-lying molecular orbitals formed between the *Ln* 5d and 6s orbitals. However, the electronic state crowding is particularly pronounced in the more Sm-rich clusters, which may be related to a level of participation of Sm 4*f* orbitals in covalent bonding with O-atoms in the clusters. In addition, we observe interesting photodetachment transition intensity dependence on photon energy (i.e., electron kinetic energy) for a number of the heteronuclear clusters as well as $Sm_3O_2^-$ and $Sm_3O_3^-$. This effect was previously observed in the Sm_2O^- and $Sm_2O_2^-$ spectra.[74] While it is a topic of ongoing theoretical treatment, we consider the new evidence from these spectra that can inform further developments in this treatment.

II. METHODS

A. Experimental details

The anion photoelectron spectrometer used in this study has been described in detail previously.[76] Cluster anions were generated using a laser ablation/pulsed molecular beam valve source[77] and a compressed Ce/$^{152}Sm_2O_3$ powder mixture (Alfa-Aesar/Trace Science) or pure $^{152}Sm_2O_3$ powder. The cluster ion masses separate in a time-of-flight mass spectrometer. Prior to colliding with an ion detector, anions were selectively photodetached with the second (532.1 nm, 2.330 eV) or third (354.7 nm, 3.495 eV) harmonic output of a Nd:YAG laser at the intersection of the ion drift tube and a second field-free drift tube, at the end of which is an electron detector. The drift times of the small fraction of photoelectrons that collided with the second dual microchannel detector assembly at the end of the drift tube were recorded on a digitizing oscilloscope. Most of the spectra were accumulated for over one million laser shots, except for the $Sm_3O_y^-$ spectra, which were collected for several hundreds of thousands to one million laser shots. All spectra were measured with laser polarizations parallel ($\theta = 0°$) and perpendicular ($\theta = 90°$) to the electron drift tube with intensities I_0 and I_{90}, respectively, in order to approximate the anisotropy parameter, $\beta(E)$,

$$\beta(E) = \frac{I_0 - I_{90}}{\frac{1}{2}I_0 + I_{90}}, \tag{1}$$

which can be related to the symmetry of the molecular orbital associated with electron detachment.

For calibration purposes, the drift times were converted to electron kinetic energy (e^-KE) by identifying common sharp transitions observed in the spectra of various Ce-based anions with similar electron affinities (EA) to the species presented below, collected using both photon energies, and setting the difference in the electron kinetic energies (e^-KE) to the fundamental energy (1.1650 ± 0.0001 eV), the difference between the energies of the second and third harmonics, using the relationship

$$\frac{2(1.1650\ \text{eV})}{m_e} = \left[\frac{\ell}{(t_{3\nu} - t_o)}\right]^2 - \left[\frac{\ell}{(t_{2\nu} - t_o)}\right]^2, \tag{2}$$

where m_e is the electron mass, $t_{3\nu}$ is the drift time of electrons associated with a selected transition observed in the spectrum obtained using 3.49 eV photon energy that can readily be correlated with a transition in the spectrum obtained with 2.33 eV, appearing at $t_{2\nu}$. The equation is solved for ℓ and plotted as a function of t_o. The intersection between

this line and other lines generated from several sets of transitions observed in 3.49 eV and 2.33 eV gives a unique ℓ and t_o, the calibration parameters necessary to compute the e^-KE values from electron drift times. The e^-KE values are related to the anion and neutral states via (2) taking into account internal energies for the anion and neutral species,

$$e^-KE = h\nu - EA - T_e^{neutral} + T_e^{anion}. \quad (3)$$

The data presented show electron counts plotted as a function of e^-BE,

$$e^-BE = h\nu - e^-KE. \quad (4)$$

The e^-BE values reflect the energy difference between the final neutral state and the initial anion state and are independent of the photon energy used.

B. Density functional theory computational details

While an accurate description of the electronic structure of these complex clusters and cluster anions is better achieved using complete active space methods, the size of the systems presented below warranted the use of less expensive methodologies, which were found to give helpful qualitative insights into homometallic[72,73] and heterometallic species[74] in previous studies. Calculations on a range of molecular and electronic structures of $Sm_xCe_{3-x}O_y$ (x = 0–3; y = 2–4) anions and neutrals were performed using the unrestricted B3LYP hybrid method within the Gaussian 09 program suite.[78] In the current study, the same functional and basis sets were used as in the previous studies: To incorporate relativistic effects on the Ce and Sm metal atoms, the Stuttgart relativistic small core atomic natural orbital basis set and corresponding effective core potential (RSC ANO/ECP) basis set with 28 core electrons and contraction of (14*s* 13*p* 10*d* 8*f* 6*g*)/[6*s* 6*p* 5*d* 4*f* 3*g*] type, developed by Cao and Dolg, was employed,[79] with the Dunning-style correlation consistent basis set aug-cc-pVTZ for the oxygen atoms.

Geometry optimization and frequency calculations on numerous initial guess structures were performed for all the anion and neutral species in a large number of spin states. Higher spin states were considered for clusters containing Sm atoms due to the larger number of unpaired 4*f* electrons. Initial guess structures included a wide range of bridge versus terminal bound *Ln* and O atoms. From this initial screening, structures with *Ln*–O–*Ln′* bridge bonds were found to be favored over structures featuring *Ln* = O terminal bonds. In addition, the only clusters that favored a three-coordinate O center were the tetroxide species. The supplementary material includes figures presenting all structures that converged for the anions and neutrals and their relative energies. Adiabatic detachment energies (ADE) of 1-e^- transitions between anion and neutral states with comparable structures were calculated from the difference between the zero point-corrected energies of the optimized anion and neutral species structures. However, as may be clear from the supplementary material, these samarium containing systems have a relatively large density of electronic states associated with which 4*f* orbitals are occupied. Editing the occupancies to force strict one-electron differences between a given anion state and a partner neutral did not always result in convergence, though there was generally a very modest change in electronic energy with changes in which 4*f* orbitals were occupied. We will see later in this paper that the availability of such accessible electronic states greatly influences the PE intensities. Detailed theoretical formalisms that account for these potentially non-adiabatic effects will be considered in a future publication.

Photodetachment spectroscopic parameters were calculated from the optimized anion and neutral structures, vibrational frequencies, and normal coordinates and were used to generate simulated spectra using home-written LabView codes for a more quantitative comparison between the experimental and computational results. Cases in which there are very large differences in anion and neutral molecular structures are treated differently since large structural changes (particularly along low-frequency, anharmonic coordinates) generally result in broad, congested electronic bands. While the complete description of these congested electronic bands may require an explicitly coupled electron-nuclear dynamical description, here we simply calculated the vertical detachment energy (VDE) from the difference in energy of the neutral confined to the structure of the anion and the optimized anion. This is the energy at which the Franck-Condon overlap is the greatest between the two charge states. Subsequently, broad Gaussian-shaped bands were generated to simulate the broad transition, with the onset of electron signals coinciding with the ADE and the maximum intensity coinciding with the VDE. More details on these procedures have been published previously.[80]

III. RESULTS AND ANALYSIS

A typical mass spectrum of the $^{152}Sm_xCe_{3-x}O_y^-$ (x = 0–3) mass region is shown in Fig. 1. The differently colored combs labeling the various oxide series with y = 1–7 correspond to different values of x. The purple comb (x = 0) indicates the pure $Ce_3O_y^-$ ions, red is $SmCe_2O_y^-$, etc. We note that in previous studies, particular stoichiometries appeared favored within an oxide series (e.g., for $Mo_xO_y^-$ clusters, $y = 2x$ and $3x$ stoichiometries were more pronounced than other compositions in the mass spectra[81]). In the case of the mixed and pure trimetallic lanthanide oxides shown in Fig. 1, the more pronounced species have different overall oxidation states. $Ce_3O_3^-$ is pronounced in the $Ce_3O_y^-$ series (purple), $SmCe_2O_4^-$ and $SmCe_2O_6^-$ are pronounced in the $SmCe_2O_y^-$ series (red), and $Sm_2CeO_2^-$ is most pronounced in the $Sm_2CeO_y^-$ series (green). The distribution of $Sm_3O_y^-$ ion intensities (blue) appears statistical.

The PE spectra of all species collected with both 2.330 eV and 3.495 eV photon energies are shown in Figs. 2–4, and graphical summaries of computational results are shown in Figs. 5–10. A comprehensive listing of all structures with respective spin states that converged in the calculations can be found in the supplementary material. The order in which the $Sm_xCe_{3-x}O_y^-$ spectra and computational results will be presented is in the decreasing oxidation state (y = 4–2). As the overall oxidation is incrementally decreased from y = 4,

the electronic structures become increasingly complex because of higher occupancy of the numerous close-lying molecular orbitals arising from the *Ln* 6*s* and 5*d* orbitals, and the number of energetically competitive structural isomers found computationally increases and the structures become increasingly floppy (*vide infra*). The approach here is to present the simplest cluster systems first and then proceed with the increasingly complex systems.

A. $Sm_xCe_{3-x}O_y^-$ (x = 0–3; y = 4, 3, 2) PE spectra

The ADE values approximated from the lowest electron binding energy feature observed in all of the spectra presented in Figs. 2–4, which are labeled X, fall between 0.64 eV and 1.11 eV. The ADE values associated with band X can be taken as the electron affinity of the neutral, assuming that the ground neutral state is accessed via the detachment of the anion present in the ion beam. The fairly narrow window of energy in which all of the EAs fall indicates that the EA is relatively insensitive to the average oxidation state (y) and Ce versus Sm composition (x). In the case of vibrationally broadened transitions, the ADE value is approximated as the lowest energy at which a sharp increase in signal from the baseline is observed. Tables I–III summarize the transition energies, including vertical detachment energies (VDE's), the electron binding energies at which the intensity of an electronic transition is the maximum (i.e., the anion and neutral have

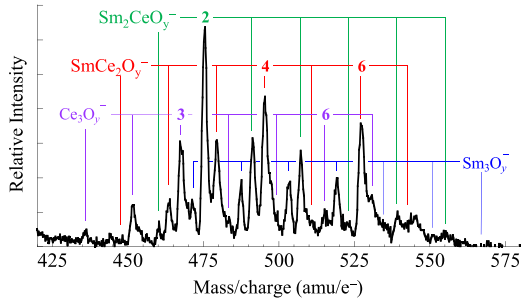

FIG. 1. Mass spectrum of cluster anions generated via laser ablation of a mixed cerium metal and $^{152}Sm_2O_3$ powder.

TABLE I. Summary of band origin positions in the PE spectra of $Sm_xCe_{3-x}O_4^-$ (x = 0–3) clusters.

			Anisotropy parameter	
Band	ADE/eV	VDE/eV	$h\nu$ = 2.33 eV	$h\nu$ = 3.49 eV
$Ce_3O_4^-$				
X	0.779(5)		1.5(3)	1.5(2)
A	1.235(8)	1.25	...	...
$SmCe_2O_4^-$				
X	0.825	0.859	1.0	1.3(1)
A	1.295	1.352	0.4(2)	0.5(2)
$Sm_2CeO_4^-$				
X	0.848	0.905	1.0(3)	0.8(1)
A	1.306	1.42	1.3(3)	0.6(3)
B	2.12	2.15		1.0(1)
$Sm_3O_4^-$				
X	0.897	0.945	1.5(1)	1.2(1)
A[a]	1.238	1.440	1.9(2)	0.5(2)
B	2.09	2.13		0.8(2)

[a]Band A is a series of resolved peaks at e^-BE = 1.238, 1.306, 1.375, 1.444, 1.490, and 1.558 eV.

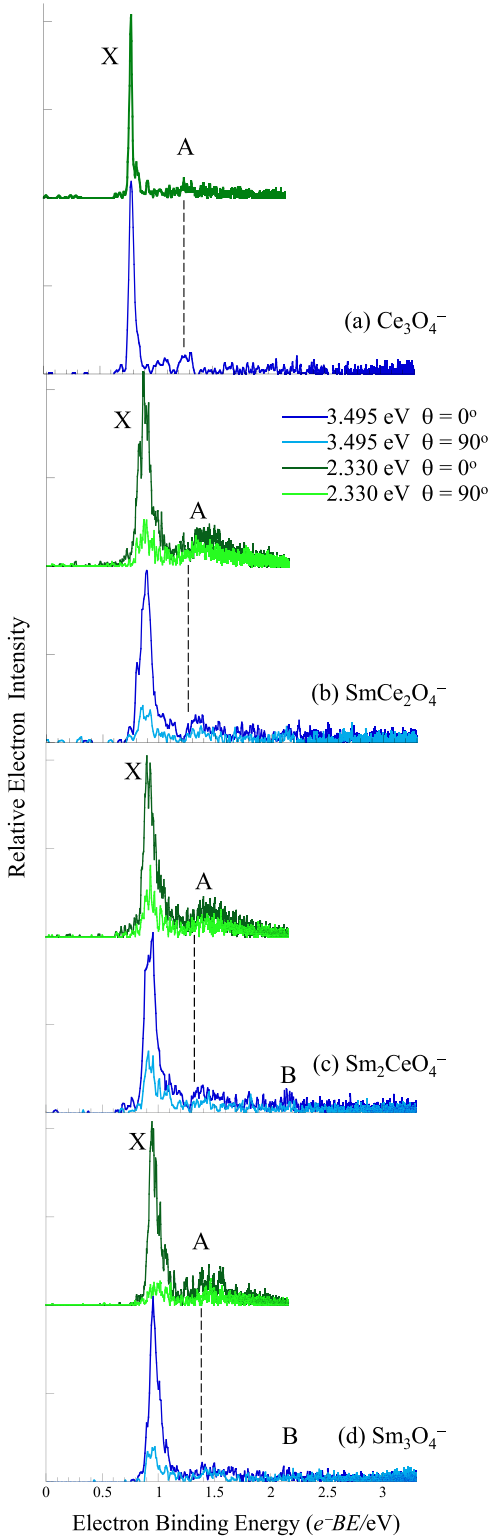

FIG. 2. PE spectra of (a) $Ce_3O_4^-$, (b) $SmCe_2O_4^-$, (c) $Sm_2CeO_4^-$, and (d) $Sm_3O_4^-$collected using 2.330 and 3.495 eV photon energies with laser polarizations parallel (dark green and blue traces) and perpendicular (light green and blue traces) to the direction of electron detection.

TABLE II. Summary of band origin positions in the PE spectra of $Sm_xCe_{3-x}O_3^-$ (x = 0–3) clusters.

			Asymmetry parameter	
Band	ADE/eV	VDE/eV	$h\nu$ = 2.33 eV	$h\nu$ = 3.49 eV
$Ce_3O_3^-$				
X	1.00(1)	1.10(1)	1.0(1)	1.2(1)
A	...	1.48(2)	0.7(1)	0.8(1)
B		2.28(3)		0.3(2)
$SmCe_2O_3^-$				
X	0.64(2)	0.73(3)	1.2(1)	1.0(1)
A	1.12(2)	1.15(20)	0.4(2)	0.7(2)
B		1.44	0.7(3)	0.7(3)
C		1.60	0.5(3)	1.2(2)
$Sm_2CeO_3^-$				
X	0.64(2)	0.77(20)	0.6(1)	0.8(1)
A		1.11(2)	1.2(1)	0.8(1)
B		1.25(3)	0.8(2)	0.8(1)
C		1.84(3)		1.0(2)
$Sm_3O_3^-$				
X	0.72(5)	0.80(2)	1.0(1)	1.1(1)
A		1.31(2)	0.6(3)	0.8(2)
B		1.47(2)	0.7(3)	0.7(2)

the greatest Franck-Condon overlap). In the case of numerous overlapping excited states, only the VDE values are reported. The anisotropy parameters for all transitions are greater than zero, meaning that the photoelectron angular distributions tend to be parallel to the detachment laser polarization.

The PE spectra of (a) $Ce_3O_4^-$, (b) $SmCe_2O_4^-$, (c) $Sm_2CeO_4^-$, and (d) $Sm_3O_4^-$ are shown in Fig. 2. The spectrum of $Ce_3O_4^-$ was presented previously[73] and is included here for direct comparison. The dark and light green traces are the spectra obtained with 2.330 eV, with laser polarization parallel to and perpendicular to the direction of electron collection, respectively. The dark and light blue traces are spectra obtained with 3.495 eV photon energy, with parallel and perpendicular laser polarization, respectively. The four sets of spectra are qualitatively very similar in appearance. This finding is consistent with the common valency anticipated for the lanthanoids noted in Sec. I. All four spectra are dominated by an intense and relatively narrow feature, labeled X, with origins ranging from 0.779 eV for $Ce_3O_4^-$, increasing slightly with the number of Sm atoms in the cluster, up to 0.897 eV for $Sm_3O_4^-$. A low intensity band appears 0.5 eV higher in energy in each spectrum. Experimental transition energies and anisotropy parameters are summarized in Table I.

Figure 3 shows the PE spectra of (a) $Ce_3O_3^-$, (b) $SmCe_2O_3^-$, (c) $Sm_2CeO_3^-$, and (d) $Sm_3O_3^-$ presented in the same format as the $Sm_xCe_{3-x}O_4^-$ spectra in Fig. 2. Again, the PE spectrum of $Ce_3O_3^-$ has been presented previously[73] and is included for direct comparison. Unlike the $Sm_xCe_{3-x}O_4^-$ spectra, the spectra of the trioxide species exhibit broader and more numerous transitions, consistent with the increased population of close-lying *Ln* 5*d* and/or 6*s*-based molecular

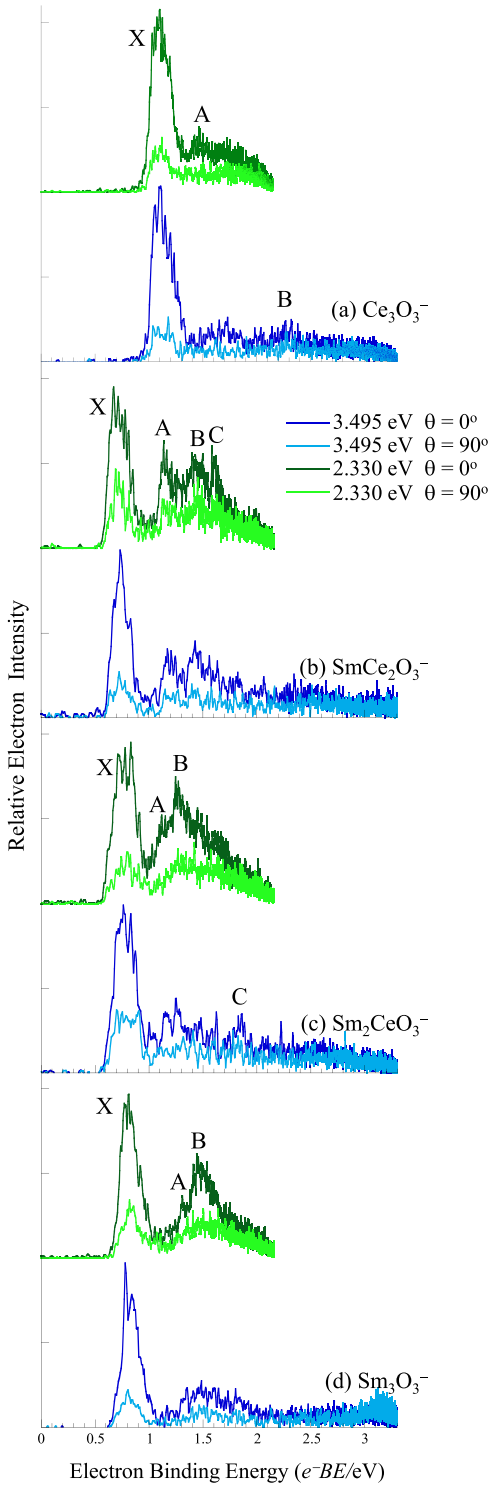

FIG. 3. PE spectra of (a) $Ce_3O_3^-$, (b) $SmCe_2O_3^-$, (c) $Sm_2CeO_3^-$, and (d) $Sm_3O_3^-$ collected using 2.330 and 3.495 eV photon energies with laser polarizations parallel (dark green and blue traces) and perpendicular (light green and blue traces) to the direction of electron detection.

orbitals. In addition, the ADE values are lower for the three Sm-containing species relative to $Ce_3O_3^-$. Table II summarizes the ADE and VDE values for band X in all four spectra, along with VDE values for all excited state bands; their origins cannot be identified unambiguously due to spectral overlap with adjacent bands. The ADE values for band X, which can be taken as the neutral EA, are 1.00 eV for $Ce_3O_3^-$,

TABLE III. Summary of band origin positions in the PE spectra of $Sm_xCe_{3-x}O_2^-$ (x = 0–3) clusters.

Band	ADE/eV	VDE/eV	Asymmetry parameter	
			$h\nu$ = 2.33 eV	$h\nu$ = 3.49 eV
$Ce_3O_2^-$				
X	0.95(5)	1.10(2)	0.9(1)	0.8(1)
$SmCe_2O_2^-$				
X	1.11(3)	1.23(2)	0.7(1)	1.0(1)
A		1.5(1)	1.2(1)	1.0(1)
B		1.85(5)		0.6(2)
$Sm_2CeO_2^-$				
X	0.95(10)	1.08(3)	0.9(1)	0.8(1)
A		1.23(3)	1.0(1)	0.8(1)
B	1.52(3)	1.56(2)	1.2(1)	0.8(2)
C	1.84(2)	1.90(2)		0.6(3)
D	2.21(2)	2.31(5)		0.9(3)
$Sm_3O_2^-$				
X	0.87(3)	1.00(5)	0.9(1)	0.8(1)
A		1.25(2)	1.0(1)	0.7(1)
B		1.55(3)	0.8(1)	0.6(2)
C		1.95(3)		0.4(3)
D		2.3(1)		0.9(3)

0.64 eV for both $SmCe_2O_3^-$ and $Sm_2CeO_3^-$, and 0.72 eV for $Sm_3O_3^-$.

The PE spectra of the three Sm-containing species exhibit a striking disparity in the relative intensities of excited state bands (labeled A, B, ...) relative to band X in the spectra obtained with 2.330 eV photon energy, when compared to the respective spectra obtained with 3.495 eV photon energy. The excited state bands are more prominent in the spectra obtained with lower photon energy. The higher intensity of the excited state transitions with lower detachment photon energy is the opposite effect expected from the decreasing photodetachment cross section with lower e^-KE.[82]

A similar effect can be seen in Fig. 4, which shows the PE spectra of (a) $Ce_3O_2^-$, (b) $SmCe_2O_2^-$, (c) $Sm_2CeO_2^-$, and (d) $Sm_3O_2^-$. The spectrum of $Ce_3O_2^-$ was presented previously[73] and is again included for direct comparison. The PE spectra of $Ce_3O_2^-$ and $SmCe_2O_2^-$ are very similar in terms of their relatively simple appearance and ADE values of their respective bands X. The broad, unresolved excited state feature labeled A in the PE spectrum of $SmCe_2O_2^-$ is modestly more intense in the spectrum obtained using 2.330 eV photon energy compared to the 3.495 analog. By contrast, the PE spectra of $Sm_2CeO_2^-$ and $Sm_3O_2^-$ are congested with more numerous close-lying, overlapping transitions, and the change in relative intensities of the excited state transitions seen when comparing spectra obtained with different photon energies is significant. Notably, bands B in the $Sm_2CeO_2^-$ and $Sm_3O_2^-$ spectra, which both appear at e^-BE = 1.55–1.56 eV, are the most intense features in both spectra obtained with 2.330 eV photon energy. The difference in the relative intensities of band A in both spectra to band X is less dramatic. Table III summarizes the transition energies for the distinct electronic transitions observed in these four spectra.

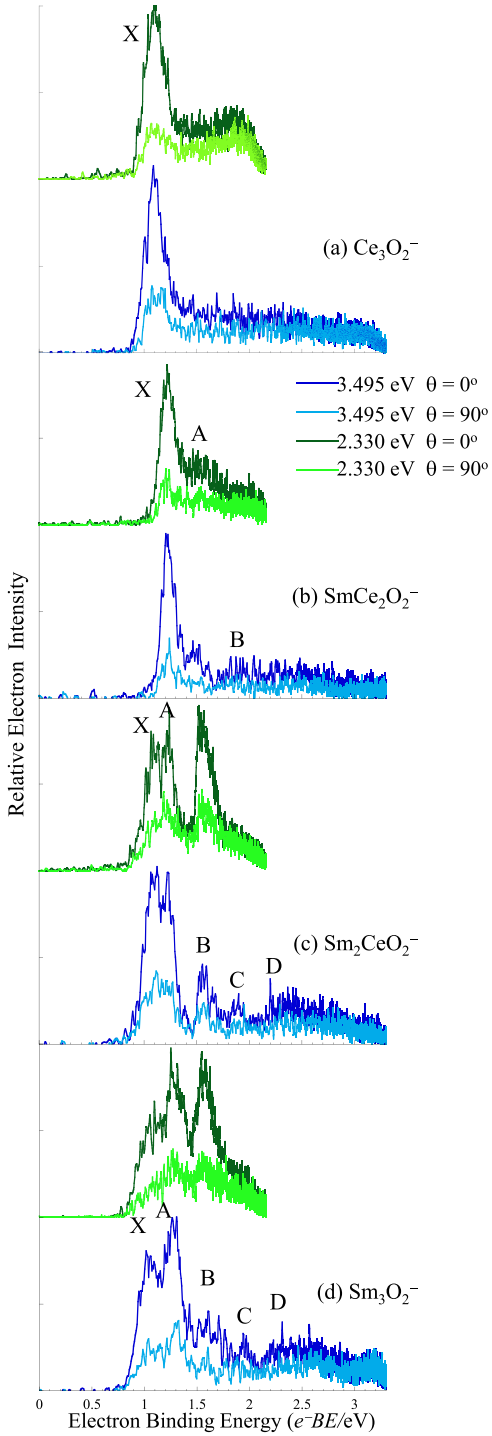

FIG. 4. PE spectra of (a) $Ce_3O_2^-$, (b) $SmCe_2O_2^-$, (c) $Sm_2CeO_2^-$, and (d) $Sm_3O_2^-$ collected using 2.330 and 3.495 eV photon energies with laser polarizations parallel (dark green and blue traces) and perpendicular (light green and blue traces) to the direction of electron detection.

B. Computational results: $Sm_xCe_{3-x}O_y^-$ (*x* = 0–3; y = 4, 3, 2) molecular and electronic structures

The lanthanoid suboxides are computationally challenging because of energetically competitive high spin and open-shell low spin states associated with ferromagnetic versus antiferromagnetic coupling between the unpaired electrons in the 4*f* subshells. For Sm-containing species, an additional

TABLE IV. Summary of computational results on $Sm_xCe_{3-x}O_4^-$/$Sm_xCe_{3-x}O_4$.

	Relative energy) (eV)	$\langle S^2\rangle$[a]	Occ. of 6*s*-based MOs
Ce_3O_4			
^3A	0.62	3.00(2)	1
^5A	0.58	6.00	
$Ce_3O_4^-$			
^6A	0.09	8.75	2
^4A	0.02	4.41(3.75)	
^2A	0.00	2.44(0.75)	
$SmCe_2O_4$			
$^7A''$	1.15	13.01(12)	~0.5
$^9A'$	0.31	20.01	
^5A	0.23	8.01(6)	
$SmCe_2O_4^-$			
$^8A'$	0.07	16.66(15.75)	2
$^6A'$	0.03	10.76(8.75)	2
$^4A''$	0.01	6.67(3.75)	2
$^{10}A'$	0.00	24.76	2
Sm_2CeO_4			
$^{13}A'$	0.52	42.04	0
$^{13}A'$	0.47	42.04	
$^{11}A''$	0.44	31.03	
$Sm_2CeO_4^-$			
^{12}A[b]	0.21	36.66	2
$^{12}A'$[c]	0.04	36.76	
$^{14}A'$	0.00	48.78	
Sm_3O_4			
^7A	0.50	17.06(12)	0
^{17}A	0.43	72.06	
$Sm_3O_4^-$			
^{16}A	0.22	64.66	2
^{18}A	0.00	80.80	

[a]In cases of significant spin contamination, the ideal value of $\langle S^2\rangle$ = S(S+1) is included.
[b]Ce 4*f* e$^-\alpha$, 6s e$^-$'s paired.
[c]Ce 4*f* e$^-\beta$, both 6s e$^-$'s α.

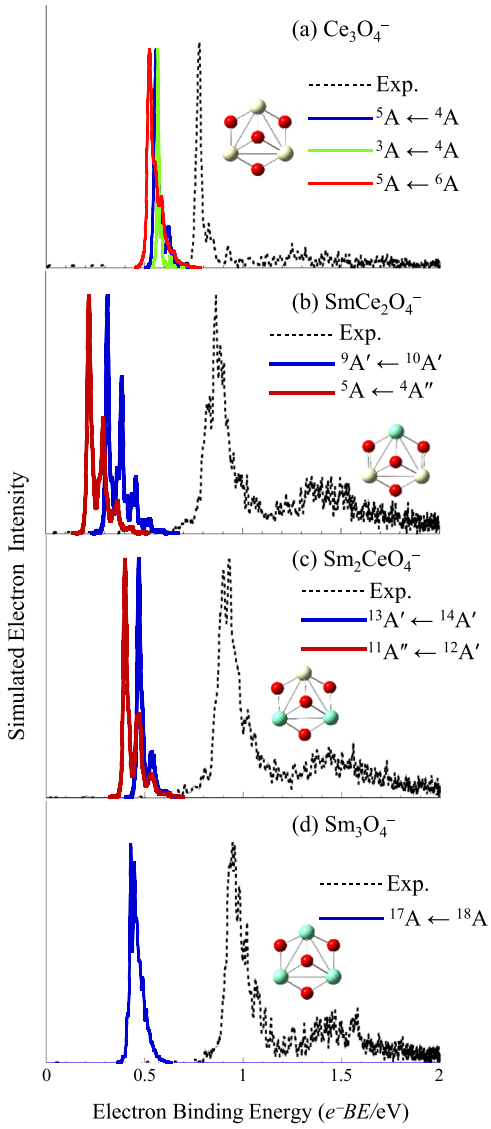

FIG. 5. Computation-based spectral simulations (solid colored traces) superimposed on the experimental PE spectrum obtained with 2.330 eV photon energy (dotted black trace) for (a) $Ce_3O_4^-$, (b) $SmCe_2O_4^-$, (c) $Sm_2CeO_4^-$, and (d) $Sm_3O_4^-$. The lowest energy anion structures are included as well. Simulation parameters and a comprehensive listing of all structures and relative energies are included in the supplementary material.

complication arises from energetically competitive $4f^5$ and $4f^6$ subshell occupancies that emerged from DFT calculations on SmO^-.[74] The combination of the ferro- and antiferromagnetic spin coupling between the individual like- and unlike atoms in any species with an Sm center results in a large number of electronic states in a narrow (<0.5 eV) energy interval, as summarized in Tables IV–VI. However, previous computational results on homometallic $Ce_xO_y^-$ clusters did provide useful qualitative insight into the electronic and molecular structures, and we again turn to the computational results to qualitatively underpin spectral interpretation.

To place the computational results in a simple context, qualitatively, if the Ce centers in all species have a singly occupied 4*f* orbital and the Sm centers have $4f^5$ subshell occupancy, both of which are favored in their respective bulk sesquioxides, the $Sm_xCe_{3-x}O_4^-$ (x = 1–3) anions should have two remaining electrons in *Ln*-local 6*s* or 5*d* orbitals. Based on previous studies on $Ce_xO_y^-$ ($y \le x$), the highest occupied orbitals should predominantly have *Ln* 6*s* character. Likewise, the $Sm_xCe_{3-x}O_3^-$ (x = 1–3) anions should have four *Ln*-6*s* or 5*d* local electrons, and $Sm_xCe_{3-x}O_2^-$ (x = 1–3) anions should have six. However, the computational results suggest Sm 4*f* subshell occupancies greater than five in a number of cases. Given that it is easy to distinguish the diffuse 6*s*- and 5*d*-based MOs from the more localized Ce- or Sm-local 4*f* and Sm–O 4*f*-2*p* bonding orbitals, we used the 6*s*- and 5*d*-based MO occupancy (the O-atoms are assumed to be $2p^6$, leaving the balance of electrons in the *Ln* 4*f* subshells) as a point of comparison between the anions and neutrals and along successive values of x in $Sm_xCe_{3-x}O_y^-$. These electron counts along with a summary of computational results are given in Tables IV–VI.

Finally, clusters with one or more Sm atoms can, in principle, have very high spin states due to parallel spins of the five or more electrons in the 4*f* subshells on each Sm center. Amongst the three *Ln* (Sm or Ce) atoms in these clusters, the

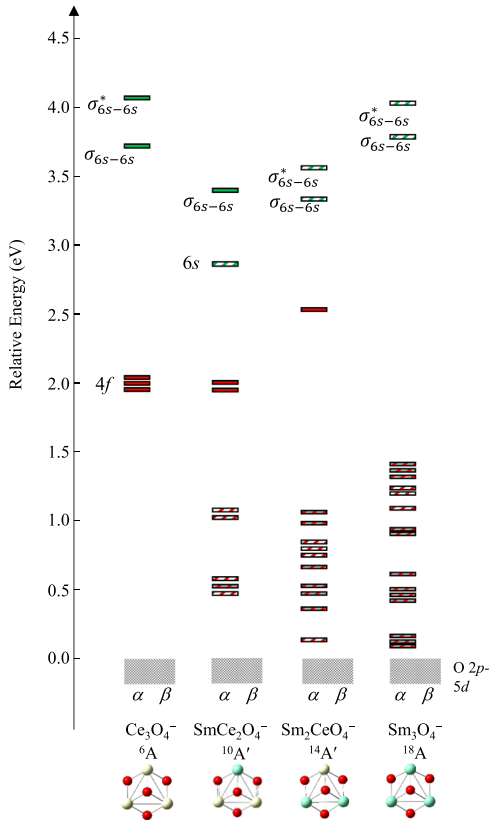

FIG. 6. Schematic of the relative energies of occupied molecular orbitals for $Sm_xCe_{3-x}O_4^-$. Solid filled shapes indicate Ce based MOs and hatch-filled shapes indicate Sm based MOs. The character of the orbitals is indicated by the colors green, red, and gray for 6*s*, 4*f*, and 2*p*-5*d*, respectively. A similar schematic showing absolute orbital energies rather than relative to the 2*p*-5*d* bonding orbitals that correlate with the bulk VB is included in the supplementary material.

4*f* electrons on one center can be parallel or antiparallel to the others, resulting in close lying higher and lower spin states. Tables IV–VI summarize how the calculations predict these ferromagnetically coupled and antiferromagnetically coupled states are competitive, and we additionally include the "ideal" S(S+1) value for spin states with $\langle S^2 \rangle$ values that indicate a high level of spin contamination due to antiferromagnetically coupled electrons. Ultimately, we look to the computational results more for a description of the *Ln* superconfigurations and point out that with the seven partially occupied 4*f* orbitals on each center being very close in energy, the true electronic states of these species must be presumed to be heavily mixed.

***y* = 4**. The $Ce_3O_4^-$ spectrum and computational results, which have been reported previously,[73] provide a convenient starting point for describing the electronic structures of this set of clusters. Figure 5(a) shows the lowest energy structure found computationally for $Ce_3O_4^-$, which is evocative of trinuclear lanthanide single molecule magnets.[83] This structure is very similar to the C_{3v} structure of $Ce_3O_4^+$ determined by Asmis and co-workers,[84] though $Ce_3O_4^-$, with two additional electrons relative to the cation, undergoes modest Jahn-Teller distortion to C_s symmetry in our calculations. The calculations, however, generally failed to assign a symmetry higher than C_1.

TABLE V. Summary of low-lying states calculated for $Sm_xCe_{3-x}O_3^-$ and $Sm_3Ce_{3-x}O_3$ (x = 0–3). Results of calculations on $Ce_3O_4^-$ and Ce_3O_4 updated from Ref. 73.

		Relative energy (eV)	$\langle S^2 \rangle$[a]	Occ. of 6*s*-based MOs
Ce_3O_3				
	book ^{3}A	0.97	3.14(2)	3
	book ^{5}A	0.94	6.05	
	ring ^{1}A	0.78	2.01(0)	3
	ring ^{5}A	0.78	6.01	
	ring ^{3}A	0.74	3.66(2)	
$Ce_3O_3^-$				
	book ^{4}A	0.05	4.78(3.75)	4
	book ^{6}A	0.00	8.77	
$SmCe_2O_3$				
	ring ^{11}A″	0.94	30.01	2
	ring ^{3}A″	0.93	5.97(2)	
	asym book ^{11}A	0.90	30.01	
	sym book ^{5}A′	0.68	8.01(6)	
	sym book ^{9}A′	0.68	20.01	
	asym book ^{7}A	0.54	13.05(12)	
	asym book ^{5}A	0.53	8.07(6)	
$SmCe_2O_3^-$				
	sym book ^{8}A″	0.11	16.84	3.5–4
	ring ^{4}A″	0.11	7.34(3.75)	
	sym book ^{10}A″	0.09	24.80	
	ring ^{10}A′	0.08	25.23	
	asym book ^{6}A	0.08	10.76(8.75)	
	asym book ^{4}A	0.04	7.02	
	asym book ^{10}A	0.00	24.84	
Sm_2CeO_3				
	asym books	>0.84		
	sym book ^{11}A′	0.54	31.72	<2
	sym book ^{13}A′	0.54	42.72	
	sym book ^{15}A′	0.53	56.02	
$Sm_2CeO_3^-$				
	asym books	>0.19		<3
	sym book ^{16}A″	0.15	63.78	
	sym book ^{10}A″	0.14	27.31(24.75)	
	sym book ^{14}A′	0.02	49.08	
	sym book ^{12}A′	0.00	36.78	
Sm_3O_3				
	Ring $^{19}A_1$	0.77	90.03	2
	Book ^{17}A″	0.73	72.75	
	Book ^{19}A′	0.72	90.04	
	book ^{7}A″	0.64	17.86	
$Sm_3O_3^-$[b]				
	Book ^{20}A″	0.28	99.8	3
	book ^{8}A′	0.18	20.86(15.75)	
	book ^{6}A″	0.03	15.19(8.75)	
	book ^{18}A″	0.00	81.17	

[a]In cases of significant spin contamination, the ideal value of $\langle S^2 \rangle$ = S(S+1) is included.
[b]The $Sm_3O_3^-$ ring structure energies are 0.30 eV and higher than the lowest book state.

Each Ce center in the structure shown in Fig. 5(a) has a singly occupied 4*f* orbital, and two electrons occupy close-lying diffuse, largely non-bonding orbitals primarily with contributions from the three Ce 6*s* orbitals.[73] Relative orbital energies are shown schematically in Fig. 6 and can be

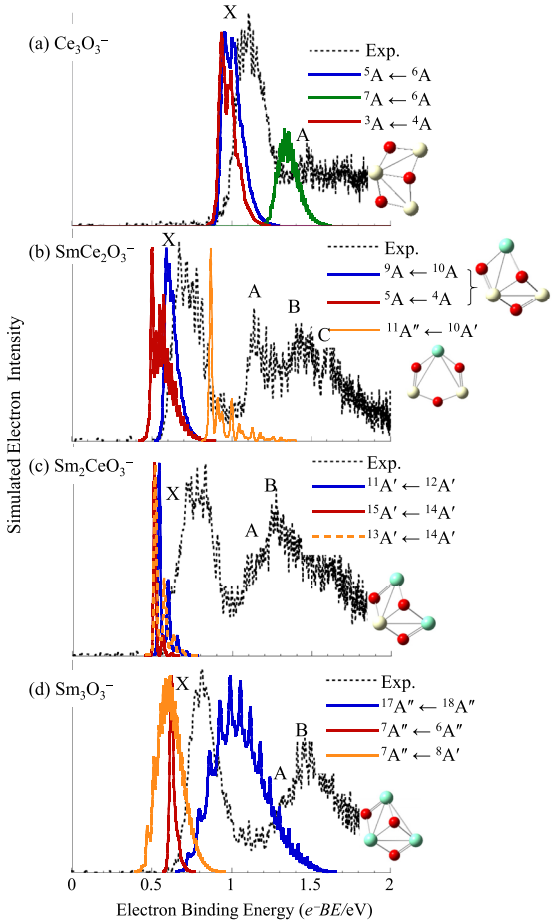

FIG. 7. Computation-based spectral simulations (solid colored traces) superimposed on the experimental PE spectrum obtained with 2.330 eV photon energy (dotted black trace) for (a) $Ce_3O_3^-$, (b) $SmCe_2O_3^-$, (c) $Sm_2CeO_3^-$, and (d) $Sm_3O_3^-$. The lowest energy anion structures are included as well. Simulation parameters and a comprehensive listing of all structures and relative energies are included in the supplementary material.

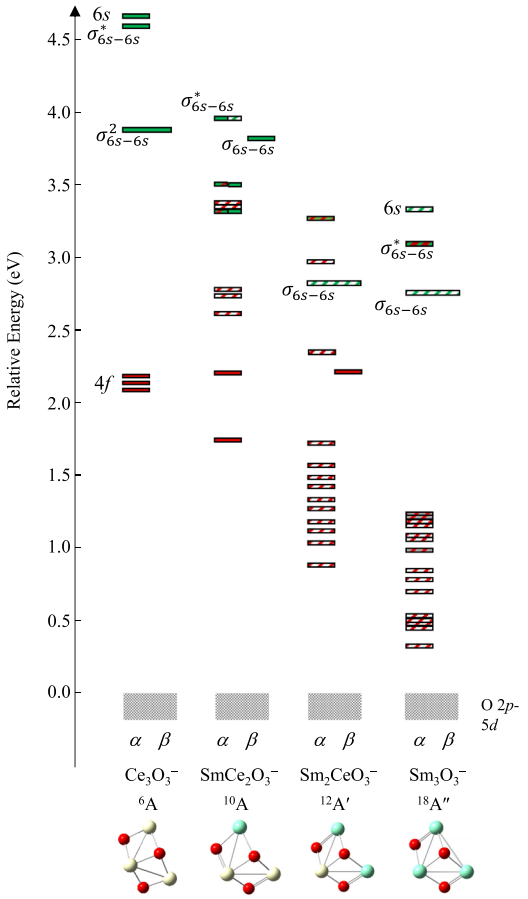

FIG. 8. Schematic of the relative energies of occupied molecular orbitals for $Sm_xCe_{3-x}O_3^-$. Solid filled shapes indicate Ce based MOs and hatch-filled shapes indicate Sm based MOs. The character of the orbitals is indicated by the colors green, red, and gray for 6*s*, 4*f*, and 2*p*-5*d*, respectively. A similar schematic showing absolute orbital energies, rather than relative to the 2*p*-5*d* bonding orbitals that correlate with the bulk VB is included in the supplementary material.

largely correlated with the bulk band structure of Ce_2O_3 in that the singly occupied Ce-local 4*f* orbitals (solid red) are within a narrow energy window, roughly midway between the predominantly O 2*p* bonding orbitals [correlating to the valence band (VB) and indicated by gray] and non-4*f* Ce-local orbitals, in this case, diffuse, 6*s* based MOs (solid green). The latter do not strictly correlate with the conduction band (CB) in Ce_2O_3 (or CeO_2), which is primarily Ce 5*d*, but as described previously,[73] the diffuse 6*s* orbitals emerge as more stable than the 5*d* orbitals when unconfined by the bulk lattice.

As summarized in Table IV, doublet, quartet, and sextet anion spin states are predicted to fall within a 0.09 eV window of energy, with a doublet state having one of the 4*f* electrons antiparallel to the other two, predicted to be lowest energy. However, these three structures are nearly identical, and the triplet and quintet neutral states (one-electron accessible from the quartet and sextet states), which are calculated to be approximately 0.6 eV higher in energy than the anions, are predicted to be nearly degenerate. This result aligns with how electrons in the 4*f* and 6*s* orbitals in CeO/CeO^- are decoupled.[71,72] Simulations based on the $^3A \leftarrow {}^4A$, $^5A \leftarrow {}^4A$, and $^5A \leftarrow {}^6A$ transitions (the $^3A \leftarrow {}^2A$ transition is not strictly one-electron allowed, though there is undoubtedly a low-lying AF-coupled ^3A neutral state not found computationally that would be one-electron accessible from the calculated ^2A state) are nearly identical in terms of transition energy and Franck-Condon profile, as shown in Fig. 5(a); spectroscopic parameters are included in the supplementary material. The calculated transition energies are approximately 0.25 eV lower than the observed transition energy, which is within the typical error between DFT-calculated and observed detachment energies.[34,44,85] Structural parameters and depictions of the orbitals and spin densities are included in the supplementary material.

The $Sm_xCe_{3-x}O_4^-$ (x = 1–3) clusters are predicted to assume the same general molecular structures. Substituting a Sm center for a Ce center results in increasing the total number of 4*f*-electrons by, minimally (*vide infra*), four, and the spin multiplicities for analogous electronic states of $Sm_xCe_{3-x}O_4^-$ increase by +4 for each incremental increase in x. The various spin states and relative energies calculated for the anions and neutrals are included in Table IV, and the relative energies of occupied orbitals are included in Fig. 6. The supplementary material includes a similar comparison of the occupied orbital energies using the actual energies rather than

TABLE VI. Summary of low-lying states calculated for $Sm_xCe_{3-x}O_2^-$ and $Sm_3Ce_{3-x}O_2$ ($x = 0$–3). Results of calculations on $Ce_3O_2^-$ and Ce_3O_2 updated from Ref. 73.

		Relative energy (eV)	$\langle S^2\rangle$[a]	Occ. of 6*s*-based MOs
Ce_3O_2				
	house ^{3}A	1.01	3.86(2)	5
	kite ^{3}A	0.99	3.63(2)	
	house ^{5}A	0.98	6.70(6)	
	kite ^{5}A	0.97	6.54(6)	
	kite ^{1}A	0.97	2.63(0)	
$Ce_3O_2^-$				
	kite ^{2}A	0.16	2.79(0.75)	6
	kite ^{4}A	0.02	4.78(3.75)	
	house ^{4}A	0.01	3.98	
	kite ^{6}A	0.01	8.80	
	house ^{2}A	0.00	2.05(0.75)	
$SmCe_2O_2$[b]				
	sym kite ^{5}A″	1.24	9.04(6)	4
	sym kite ^{9}A	1.20	21.05	
	sym kite ^{7}A″	1.06	14.02(12)	
	sym kite ^{3}A	1.05	6.01(2)	
	sym kite ^{11}A″	0.94	30.02	
$SmCe_2O_2^{-\beta}$				
	sym kite ^{4}A′	0.07	6.77(3.75)	5
	sym kite ^{8}A	0.04	16.78	
	sym kite ^{6}A′	0	10.78(8.75)	
Sm_2CeO_2				
	asym kite ^{17}A	1.38	72.01	3
	house ^{15}B$_1$	1.19	56.02	
	house ^{13}B$_1$	1.17	43.02	
	house ^{11}B$_1$	1.14	32.02(30)	
	asym kite ^{13}A	0.89	43.02	
	asym kite ^{11}A	0.87	32.02(30)	
	asym kite ^{15}A	0.84	56.03	
$Sm_2CeO_2^-$				
	house ^{10}A	0.36	27.78(24.75)	4
	house ^{14}B$_2$	0.32	49.77	
	house^{16}B$_2$	0.28	63.78	
	house ^{12}A$_2$	0.28	37.77(35.75)	
	asym kite ^{2}A	0.25	6.79(0.75)	
	asym kite ^{10}A	0.15	27.73(24.75)	
	asym kite ^{12}A	0.00	37.74(35.75)	
Sm_3O_2				
	kite ^{17}A	0.69	73.63(72)	3
	kite ^{21}A	0.55	110.03	
	house ^{7}A	0.47	18.03(12)	
	house ^{19}B$_2$	0.46	90.03	
$Sm_3O_2^-$				
	house ^{16}A$_2$	0.37	65.81(63.75)	4-5
	kite ^{22}A	0.21	120.77	
	house ^{20}A$_1$	0.17	99.79	
	house ^{18}A$_2$	0.00	81.78(80.75)	

[a]In cases of significant spin contamination, the ideal value of $\langle S^2\rangle = S(S+1)$ is included.
[b]Structures with Ce_2O_2 trapezoid units with Sm bound to an O atom in one of the Ce–O–Ce bridge bonds (sym kite) are 0.6 eV and 0.5 eV more stable, respectively, for anions and neutrals than $CeSmO_2$ trapezoid units with Ce bound to an O-atom in the Ce–O–Sm bridge (asym kite).

energies relative to the VB-like orbitals. Among this series of anions, the singly occupied Ce-local 4*f* orbitals (solid

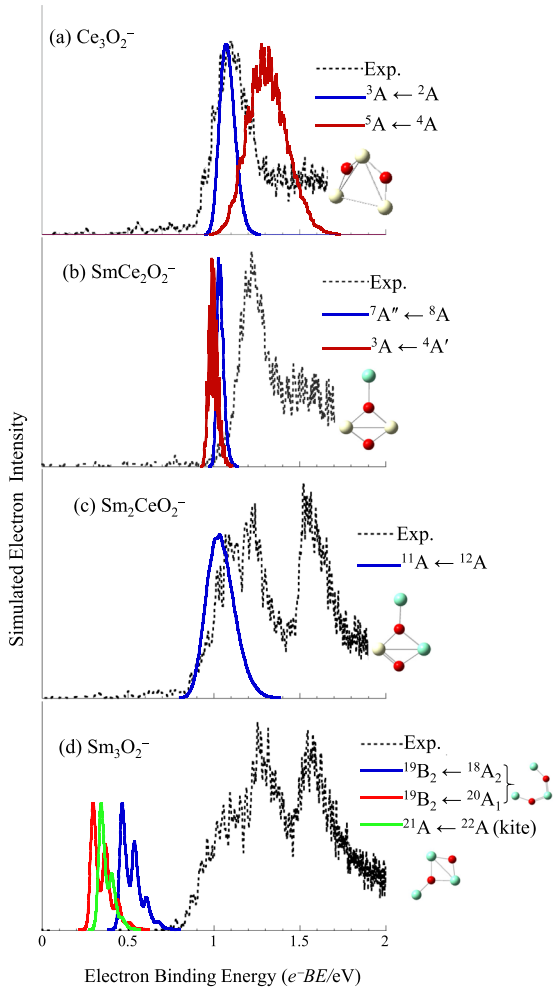

FIG. 9. Computation-based spectral simulations (solid colored traces) superimposed on the experimental PE spectrum obtained with 2.330 eV photon energy (dotted black trace) for (a) $Ce_3O_2^-$, (b) $SmCe_2O_2^-$, (c) $Sm_2CeO_2^-$, and (d) $Sm_3O_2^-$. The lowest energy anion structures are included as well. Simulation parameters and a comprehensive listing of all structures and relative energies are included in the supplementary material.

red) lie between the orbitals correlating with the VB (gray) and the CB (green), while the introduction of Sm centers also introduces numerous Sm-local 4*f* orbitals (hatched red) closer in energy to the VB analogs. In addition, 4*f*-covalency with O 2*p* orbitals is also predicted (hatched red and gray), an effect previously reported by Bowen and co-workers in studies on SmB_6^-/SmB_6.[86] These relative occupied orbital energies are evocative of the bulk band structure of Sm_2O_3, in which the 4*f* band is energetically embedded at the top of the VB.[87,88]

Calculations on the lowest energy structure found for $SmCe_2O_4^-$ [Fig. 5(b)] predict very close-lying octet, sextet, and quartet spin states within 0.08 eV of the lowest lying ^{10}A′ electronic state, as summarized in Table IV. The ^{10}A′ state is analogous to the ^{6}A state of $Ce_3O_4^-$, in which the two electrons in the diffuse 6*s* based orbitals are parallel to each other and the 4*f* electrons. An important difference with the $SmCe_2O_4^-$ cluster is that the Sm atomic 6*s* orbital is not degenerate with the two degenerate 6*s* orbitals on the Ce atoms, and the three resulting MOs can be described as a Sm 6*s* orbital and the $\sigma_{(Ce\ 6s\ -\ Ce\ 6s)}$ and $\sigma^*_{(Ce\ 6s\ -\ Ce\ 6s)}$ combinations

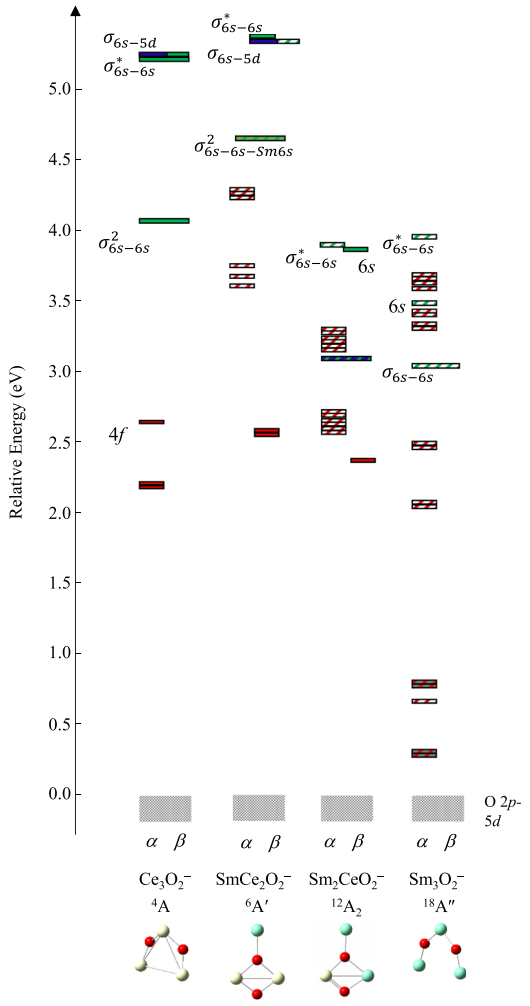

FIG. 10. Schematic of the relative energies of occupied molecular orbitals for $Sm_xCe_{3-x}O_2^-$. Solid filled shapes indicate Ce based MOs and hatch-filled shapes indicate Sm based MOs. The character of the orbitals is indicated by the colors blue, green, red, and gray for 5*d*, 6*s*, 4*f*, and 2*p*-5*d*, respectively. A similar schematic showing absolute orbital energies, rather than relative to the 2*p*-5*d* bonding orbitals that correlate with the bulk VB is included in the supplementary material.

of the two identical Ce 6*s* orbitals. The Sm 6*s* orbital is 0.5 eV lower in energy from the diffuse bonding formed between the two Ce 6*s* orbitals, as shown schematically in Fig. 6 (hatched green; depictions of the orbitals and their energies are included in the supplementary material). The Sm 6*s* orbital and the $\sigma_{(Ce\ 6s\ -\ Ce\ 6s)}$ orbital are both singly occupied in all four anion states included in Table II, with the different spin states arising from different electron spins in the $\sigma_{(Ce\ 6s\ -\ Ce\ 6s)}$ and Ce 4*f* orbitals.

The lowest energy transitions, in principle, should involve detachment of the electron from the Ce 6*s*-based σ orbital. However, the calculated ADE values associated with the detachment of the close-lying ^{4}A″ and ^{10}A′ anion states, accessing the neutral ^{5}A and ^{9}A′ states, are 0.22 eV and 0.31 eV, respectively, much lower than the observed detachment transition energy, 0.825 eV. In addition, a survey of the occupied MOs in both the anion and neutral suggest that these transitions are not strictly one-electron. The HOMO of the neutral is an Sm-local 4*f*-like orbital, and while it appears to be modestly hybridized with the 6*s* orbital, it is markedly less diffuse than the Sm-local 6*s* HOMO-1 singly occupied in the anion. A side-by-side comparison of the $SmCe_2O_4$ anion and neutral orbitals and energies along with a comparison with Ce_3O_4 neutral orbitals are included in Figs. S17 and S18 of the supplementary material. The lowest energy unoccupied neutral orbitals are the $\sigma_{(Ce\ 6s\ -\ Ce\ 6s)}$, $\sigma^*_{(Ce\ 6s\ -\ Ce\ 6s)}$, and the Sm 6*s* orbital, in the order of increasing energy, the first and third of which are occupied in the anion. The extra electron occupying the Sm-4*f* orbital is accompanied by destabilization of the Sm 6*s* orbital and elongation of all three Sm–O bond lengths. The orbital occupancy of the higher-lying ^{7}A′ neutral state that converged in calculations includes a singly occupied, diffuse, Sm-6*s* orbital. However, simulations based on transitions to this excited state show a more extended progression in the highest frequency stretch modes.

We note that ongoing work by our labs on europium oxide and related species has found qualitatively different MO descriptions that appear to be dependent on subtle variations in model chemistry.[89,90] Such model chemistry differences include the choice of ECP or all-electron metal basis sets and the choice for treating relativistic effects (i.e., implicit treatment of scalar and/or spin-orbit contributions using ECPs, explicit treatment using the Douglas-Kroll-Hess approach, etc.). In particular, the energy and occupation of the Eu 6*s* based MO varies with such changes relative to the energy of the 4*f* manifold. In addition to suggesting different interpretations of photodetachment, these model chemistry variations also yield significant differences in Franck-Condon simulations to high-energy neutral states. The implications of this disagreement between experimental and computational results will be examined in more detail below. As noted earlier, the relatively high density of spin-states available for the samarium-based systems makes it highly likely that the initial anionic state in the experiment is prepared as a wavepacket state that is a combination of multiple spin states. This is quite similar to the case already noted in Ref. 74 and will be treated in greater theoretical detail in a future publication and may account for the poor agreement between the molecular orbitals for the anionic and neutral systems discussed above.

Calculations on $Sm_2CeO_4^-/Sm_2CeO_4$ and $Sm_3O_4^-/Sm_3O_4$ show a similar discrepancy in the predicted and observed adiabatic transition energies, and in both cases, the anions have two electrons occupying orbitals having significant 6*s* character, while the neutrals have zero (Table IV). That is, transitions between the lowest energy anion and neutral electronic states found computationally are not strictly one-electron allowed. The two equivalent Sm centers in the Sm_2CeO_4 neutral therefore have $4f^{5.5}$ subshell occupancy, and on average, the Sm centers in the Sm_3O_4 neutral have $4f^{5.33}$ subshell occupancy. The Ce 4*f* subshell occupancy is unambiguously 1 for all species with a Ce center (depictions of the molecular orbitals are included in the supplementary material). While the transitions between the lowest lying anion and neutral states of Sm_2CeO_4 and Sm_3O_4 are clearly not one-electron, simulated vibrational manifolds based on the vibrational frequencies and normal coordinate displacements from the anion and neutral structures

[Figs. 5(c) and 5(d)] are in fair agreement with the profile of their respective spectra. The lowest lying states for the anions and neutrals are summarized in Table IV, with a more comprehensive compilation of computational results included in the supplementary material.

In bulk Sm_2O_3, the $4f^6$ state arising from the promotion of an electron from the VB to the Sm 4*f* sub-band lies within the traditional band gap.[87] For these small clusters, which are suboxide relative to the bulk, the $4f^6$ subshell occupancy, rather than the $4f^5$ 6*s* occupancy (analogous to promotion to the CB rather than $4f^6$), could therefore be expected to be most stable, raising the question of the validity of the computational results suggesting that the $4f^5$ 6*s* Sm superconfiguration is more stable in $Sm_xCe_{3-x}O_4^-$ anions. However, the excess charge may be stabilized by Sm $4f^5$ subshell occupancy, which increases the effective nuclear charge on the Sm centers, stabilizing the occupancy of the diffuse Ce and/or Sm 6*s*-based molecular orbitals. For context, the Sm centers in the ground electronic states of SmO and SmO^-, in which Sm is in a lower oxidation state than the tetroxide clusters described here, are in $4f^5$ 6*s* and $4f^5$ $6s^2$ superconfigurations, respectively.

The striking disagreement between computed and observed detachment energies raises critical questions regarding the qualitative validity of the calculations. However, if the results on the neutral species are correct, the disagreement could simply reflect the inability to converge excited $4f^5$ states and that these excited states are those actually accessed from the initial anion states. It is not uncommon in metal and metal suboxide systems for the neutral ground state to be inaccessible via one-electron detachment from the anion ground state, with atomic Ce being an example.[91] In any event, these results strongly suggest that further theoretical study is necessary. Such work, including new methodological developments, is ongoing in our labs.

***y* = 3**. Figure 7 summarizes computational results on $Sm_xCe_{3-x}O_3^-/Sm_xCe_{3-x}O_3$ (x = 0–3) with the lowest energy structures for each species shown alongside simulations generated from the calculated structural parameters (included in the supplementary material, along relative energies of other structures and spin states). Again, multiple close-lying spin states were calculated to be energetically competitive for each of these structures, with the lowest energy states and their Ce and/or Sm 6*s* based MO occupancies summarized in Table V. Calculations on $Ce_3O_3^-$ were presented previously, though we have generated several additional simulations based on additional spin states that converged in the current study. In general, the calculated detachment energies and transition profiles are in reasonable agreement with the experimental spectra, and low-lying anion states and low-lying neutral states can be connected by one-electron transitions.

The $Ce_3O_3^-$ anions converged exclusively in the book structure shown, with the open ring structure slightly energetically favored by the neutral.[73] By contrast, $SmCe_2O_3^-$ ring and asymmetric book structures (Sm center on the book corner) are energetically competitive: The lowest energy spin state of the ring structure [shown in Fig. 7(b)] is calculated to be within 0.1 eV of the lowest energy spin state of the asymmetric book structure for the anion. Neutral book structures are approximately 0.4 eV more stable than the open ring structures, which corresponds to a higher predicted ADE value, as can be seen in the simulation included for the open ring structure shown in Fig. 7(b). Symmetric book structures, with the Sm in the central position, are approximately 0.1–0.15 eV higher in energy for the anion and neutral, respectively. Since the central atom in the book structure is bound to three O-atoms, a Ce atom in that central position is favored because Ce–O bonds are stronger than Sm–O bonds.[92,93] Simulations based on these various states and structures support the presence of the asymmetric book structure.

For this same reason, the symmetric book structure is favored by $Sm_2CeO_3^-$ shown in Fig. 7(c) (again, Ce in the central position of the book). The open ring structure and the asymmetric book structure (Ce on a corner position) are less stable by approximately 0.2–0.3 eV for the anion and neutral, respectively. Simulations based on the symmetric book predict less vibrational congestion than what is observed, suggesting that some asymmetric book structure may be present; the calculated ADE values for both are in fair agreement with the observed transition energy. Calculations on $Sm_3O_3^-/Sm_3O_3$ predict that the book structure is 0.3 eV more stable than the open ring structure for the anion and 0.13 eV more stable for the neutral. High and relatively low spin states arise from either parallel or antiparallel spins of the 4*f* electrons on the central Sm center relative to the two corner Sm 4*f* electrons. Simulation parameters for all simulations shown are included in the supplementary material.

Figure 8 shows the evolution of the $Sm_xCe_{3-x}O_3^-$ electronic structures with x. We note here that a general description of orbital energies and occupancies for the different structural isomers are very similar (depictions of the MOs are included in the supplementary material). As calculated for the tetroxide series, the occupied Sm-4*f* orbitals (hatched red) of $Sm_3O_3^-$ and $Sm_2CeO_3^-$ are predicted to be energetically close to the orbitals that correlate with the VB (gray) of the bulk sesquioxide, and in $Sm_3O_4^-$, with several of the 4*f* orbitals appearing to be involved in covalent bonding with the O-atoms (hatched red and gray). By contrast, the occupied 4*f* orbitals in the $SmCe_2O_3^-$ anion lie energetically above the two singly occupied Ce 4*f*-local orbitals (solid red). Additionally, while all anions in the tetroxide series had the same number of electrons occupying diffuse Ce and/or Sm 6*s*-based MOs, the $SmCe_2O_3^-$ and $Sm_2CeO_3^-$ anions have three (rather than four, as in $Ce_3O_3^-$), or slightly less than three, taking into account 4*f*-6*s* hybridization (hatched red and green). $Sm_3O_3^-$ has an electronic structure more similar to $Ce_3O_3^-$, with 4 electrons in the Sm 6*s*-based orbitals (hatched green), though one also exhibits more 4*f*-6*s* hybridization. A side-by-side comparison of the $Ce_3O_3^-$ and $Sm_3O_3^-$ frontier orbitals is included in Fig. S19 of the supplementary material. Neutral electronic structures have the same 4*f* subshell occupancies as their anionic counterparts, with one less electron occupying the diffuse orbitals.

***y* = 2**. Figure 9 shows a summary of computational results on the $Sm_xCe_{3-x}O_2^-$ species, again, with the previously reported results on $Ce_3O_2^-/Ce_3O_2$ included for

direct comparison [the simulations shown in Fig. 8(a) were not previously reported]. The relative energies of the most competitive spin states for the various structures are summarized in Table VI, along with the diffuse Ce and/or Sm 6s-based MO occupancies. In these more reduced systems, 5*d*-based MOs are also occupied, and these electrons are included in the count. We note here that the calculations on this dioxide series have the additional challenge of very floppy molecular structures, so the results should be treated with extra caution.

Two structural isomers, house and kite, were calculated to be nearly isoenergetic for $Ce_3O_2^-$, while the kite structures emerge more definitively as the lowest energy isomer for both $SmCe_2O_2^-$ and $Sm_2CeO_2^-$. In both the heterometallic cases, the least coordinated kite's tail position is occupied by a Sm center, which is, again, less oxophilic than Ce.[92,93] The calculated transition energies and band profiles for both mixed species are in reasonable agreement with the observed ground state transitions.

Calculations on $Sm_3O_2^-/Sm_3O_2$ predict that the house structure is more stable than the kite structure by 0.21 eV. However, the calculated ADE values do not agree with the experimental spectrum. The simulation based on the higher energy kite structure is similarly unsatisfactory. The appearance of the $Sm_3O_2^-$ PE spectra taken both with 3.495 eV and 2.330 eV are is similar to the $Sm_2CeO_2^-$ spectra [Figs. 4(d) and 4(c), respectively] with the main differences being the slightly lower ADE values and broader bands X and A in the $Sm_3O_2^-$ spectra. The spectral similarities suggest similar molecular and electronic structures for $Sm_2CeO_2^-/Sm_2CeO_2$ and $Sm_3O_2^-/Sm_3O_2$. However, the plethora of structures and spin states attempted in calculations on $Sm_3O_2^-/Sm_3O_2$ (see the supplementary material) are all inconsistent with the observed spectrum. Bi-pyramidal structures with the O-atoms situated above and below a Sm_3 triangle failed to converge but were energetically competitive before failing. We therefore restrict the analysis of the computational results to the heterometallic systems.

Figure 10 shows the evolution of the electronic structures of the dioxide cluster anions, with depictions of the orbitals in the supplementary material. Again, for species, Ce 5*d*-based or 5*d*-6*s* hybridized MOs are occupied, indicated in blue. For both heterometallic species, the occupied Sm-local 4*f* orbitals lie above the Ce-local 4*f* orbital(s). Overall, as the clusters become less oxidized, the Sm-local 4*f* orbitals are destabilized and more so in the Ce-rich heterometallic clusters. However, the Sm $4f^6$ subshell occupancy is still maintained for the single Sm center in $SmCe_2O_2^-$ and both Sm centers in $Sm_2CeO_2^-$.

As with the trioxide series (and in contrast to the tetroxide series), in the $Sm_xCe_{3-x}O_2^-/Sm_xCe_{3-x}O_2$ progression with incremental increases in x, the number of electrons in the diffuse orbitals decreases by 1. The Ce 4*f* subshell occupancy remains unambiguously at 1, and the Sm centers assume a $4f^6$ subshell occupancy. While calculations on $Sm_3O_2^-/Sm_3O_2$ did not compare well with the observed spectrum, they predict that the Sm subshell occupancy is between 5 and 6. As noted above, the spectra of $Sm_2CeO_2^-$ and $Sm_3O_2^-$ suggest very similar electronic structures, which would imply on average a lower Sm 4*f* subshell occupancy in $Sm_3O_2^-$ than in $Sm_2CeO_2^-$.

IV. DISCUSSION

The combination of experimental and computational results presented above reveals the exceptional electronic complexity of these $Sm_xCe_{3-x}O_y^-/Sm_xCe_{3-x}O_y$ ($x = 0$–3; $y = 2$–4) suboxide species. There are three interesting trends in particular that have emerged: First, the variations in relative excited state transition intensity with photon energy, observed primarily for x = 1–3, y = 3, 2, become increasingly dramatic with the more Sm-rich and O-deficient species. Second, the Sm centers in these various species present different x and y-dependent 4*f* subshell occupancies, with increased occupancy favored in the heterometallic clusters and more reduced clusters. In the case of the species closest to bulk stoichiometry ($Sm_xCe_{3-x}O_4^-/Sm_xCe_{3-x}O_4$), this effect appears to be charge-state dependent. Third, energy of the Sm 4*f* subshell systematically changes relative to the O 2*p*-predominant bonding orbitals that correlate with the bulk VB. The stability of the subshell increases both with increasing oxidation and proportion of Sm atoms. The energy of the Ce 4*f* occupied orbitals relative to the O 2*p* bonding orbitals remains fairly constant. These three effects will now be discussed in greater detail, followed by a comment on the computational results in general.

A. Sm 4*f* subshell occupancy

As noted above, the chemistry of the lanthanoids is similar because, generally, the contracted, largely nonbonding 4*f* orbital occupancy increases incrementally with the atomic number across the lanthanoid row in the periodic table. The Ln_2O_3 sesquioxide materials favored by most lanthanoids have partially filled, narrow 4*f* bands within the conventional band gaps, though in the case of Sm_2O_3, this band lies energetically at the top of the VB.[3,94–97] The $Sm_xCe_{3-x}O_4^-/Sm_xCe_{3-x}O_4$ tetroxide clusters behave differently from the $Sm_xCe_{3-x}O_3^-/Sm_xCe_{3-x}O_3$ and $Sm_xCe_{3-x}O_2^-/Sm_xCe_{3-x}O_2$ clusters, and we address their electronic structure first. The superconfiguration description of the *Ln* centers in all four $Sm_xCe_{3-x}O_4^-$ anions have 4*f* subshell occupancies that align with the sesquioxide band structure, with the two excess electrons occupying the highly diffuse *Ln* 6*s*-based MOs. Again, these diffuse orbitals are different from the traditional Ln 5*d* conduction band: In these very small systems, the delocalized 6*s* orbitals are apparently stabilized relative to the bulk because they are not confined by an infinite lattice. The computational results show that the Sm-containing neutral analogs have higher 4*f* subshell occupancy (the Sm center in $SmCe_2O_4$ has $4f^6$, while the multiple Sm centers in Sm_2CeO_4 and Sm_3O_4 share the additional 4*f* electron), which is not surprising considering that the $4f^6$ bulk state in the sesquioxide lies within the traditional band gap.[87] The prospect of switching the relative stability of the $4f^5$ and $4f^6$ subshell occupancies with charge in these localized systems is interesting because of the fairly significant impact on the Sm–O bond strength and potential change in the magnetic moment. In effect, donation

of one electron to the neutral results in a change of +2 electrons in the diffuse orbitals that correlates with the CB of the bulk.

The $Sm_xCe_{3-x}O_3^-/Sm_xCe_{3-x}O_3$ and $Sm_xCe_{3-x}O_2^-/Sm_xCe_{3-x}O_2$ clusters do not exhibit the charge-state dependent Sm 4*f* subshell occupancy. We first consider the $Sm_xCe_{3-x}O_3^-/Sm_xCe_{3-x}O_3$ series, the neutrals of which feature *Ln* centers in the same formal oxidation states as the well-characterized CeO and SmO diatomic molecules, which favor the $4f\ 6s$ and $4f^5\ 6s$ superconfigurations, respectively[71] (Ref. 71 refers to these diffuse, slightly polarized 6*s* orbitals as the σ^* orbital). Neutral Ce_3O_3 has an electronic structure that is easily related to a trimer of CeO diatomic molecules, in which there are three electrons in the 6*s*-based orbitals (four in the anion) and three electrons in distinctly non-bonding 4*f* orbitals. Neutral Sm_3O_3 has two electrons occupying diffuse 6s-like orbitals, an average $4f^{5.33}$ subshell occupancy on each Sm atom. On the other hand, the Sm centers in neutral $SmCe_2O_3$ and Sm_2CeO_3 are more distinctly $4f^6$. This effect can be rationalized in the following manner: The bulk Ce_2O_3 VB is lower in energy than the bulk Sm_2O_3 VB, an effect reflected out in the calculations on the cluster systems (analogs to Figs. 6, 8, and 10, with orbital energies plotted on an absolute scale rather than relative to the highest energy O 2*p*-predominant MO). In the heterometallic oxide clusters, the stronger bonding between Ce and the limited number of O-atoms results in an inherent asymmetry, with Ce being more strongly bound to the limited O atoms at the expense of Sm. The Sm–O ligand field stabilized $4f^5\ 6s$ superconfiguration is bond-length dependent, with longer bond lengths resulting in the stabilization of the $4f^6$ subshell occupancy relative to the $4f^5$ subshell occupancy.

A similar picture emerges within the $Sm_xCe_{3-x}O_2^-/Sm_xCe_{3-x}O_2$ series, in which the Ce center unambiguously maintains the singly occupied, ligand field favored 4*f* subshell occupancy, while for both heterometallic clusters, the Sm center unambiguously favors the $4f^6$ subshell occupancy. The Sm centers in the Sm_3O_2 anion and neutral, on average, lie between $4f^5$ and $4f^6$. So, while the more reduced homometallic samarium oxide systems exhibit Sm $4f^{5+\delta}$ ($\delta \approx 1/3$), on average, only the heterometallic oxides feature the Sm—O bond weakening $4f^6$ occupancy. The implication of this finding is that Sm dopants in cerium oxide could generate a local disruption in the *Ln*–O bonding network. This effect may play a role in the increased ionic conductivity of Sm-doped ceria.

B. Occupied Sm 4*f* orbital energies

The computational results again suggest different trends in electronic structures for the tetroxide species when compared to the tri- or di-oxide species, though in terms of the Sm 4*f* band energy, the distinction lies primarily with the $Sm_xCe_{3-x}O_4^-$ (x = 1–3) series of anions. As noted above, the electronic structures of the $Sm_xCe_{3-x}O_4^-$ (x = 0–3) anions are evocative of the bulk sesquioxide band structure, with the occupied Sm-local 4*f* orbital energies close to the orbitals correlating with the VB, and the singly occupied Ce-local 4*f* orbitals (x = 0–2) situated midway between the VB and CB. However, in the *neutral* $Sm_xCe_{3-x}O_4$ clusters, the Sm 4*f* band is destabilized relative to the anions, an effect that is likely related to the $4f^{5+\delta}$ ($1/3 < \delta \leq 1$) subshell occupancy. Given this rationalization and the discussion on the Sm 4*f* subshell occupancy in Sec. IV A, the computational results on the $Sm_xCe_{3-x}O_3^-$ and $Sm_xCe_{3-x}O_2^-$ series follow suit. That is, in these series, the Sm 4*f* subshell occupancies for the heterometallic species are greater than those of the homometallic species, with the higher occupancy resulting in an overall destabilization of the occupied Sm 4*f* orbitals.

This effect, again, is consistent with the $4f^6$ state of bulk Sm_2O_3 lying energetically close to the CB, but within the traditional band gap, in contrast to the energy of the $4f^5$ ground state. The calculations suggest that the Sm 4*f* band energy can be tuned with the specific $Sm_xCe_{3-x}O_y^-/Sm_xCe_{3-x}O_y$ cluster composition, which affects the $4f^{5+\delta}$ ($1/3 < \delta \leq 1$) Sm occupancy. Figures 8 and 10 show clear trends in the occupied Sm 4*f* orbital energies: With increasing x (which incrementally decreases δ in the $4f^{5+\delta}$ subshell occupancy), the occupied Sm-local 4*f* local orbital energies incrementally decrease relative to both the Ce local 4*f* orbital energy and approach the VB orbital energies. Concomitantly, comparing $Sm_xCe_{3-x}O_3^-$ to $Sm_xCe_{3-x}O_2^-$, the occupied Sm-local 4*f* orbital energies are incrementally lower in the trioxides than the dioxides. These systems raise the prospect of tunable Sm 4*f* band energies, while the Ce 4*f* band remains relatively unchanged.

C. Relative intensities of transitions to excited states

We had previously reported the observation of photon energy dependent relative intensities of excited state transitions in the spectra of small homometallic Sm_2O^- and $Sm_2O_2^-$,[74] and in the current study, the effect has also been observed in heterometallic Sm–Ce oxides. We proposed that the photoelectron and neutral were strongly coupled in the initial stages of the photodetachment process and the time-evolution of the (electron + neutral) results in the population of excited states of the neutral. The effect is necessarily more pronounced when the electron is closer to the threshold due to the prolonged strong interactions. The strong coupling is associated with the exceptionally high density of states that arise from the larger number of microstates in the $4f^5$ or $4f^6$ subshell occupancy compared to the Ce 4*f* subshell occupancy; homometallic $Ce_xO_y^-$ cluster PE spectra do not exhibit this effect.

In the case of the reduced $Ce_3O_2^-$ cluster, the spectrum surprisingly does not reflect the fairly high density of low-lying electronic states arising simply from the six electrons occupying both Ce 6*s*- and 5*d*-based molecular orbitals, which should be close in energy. The relatively simple appearance of the spectrum, compared to the very congested PE spectrum of its $Sm_3O_2^-$ congener, could suggest that the spectrum of the former may be affected by "shake-down" transitions. However, only (and most of) the Sm-containing clusters exhibit this striking photon energy dependent intensity variation. The new results presented here also suggest that the energetic crowding of open, close-lying 5*d* and 6*s* based molecular orbitals in clusters with Sm atoms contributes to the effect, given

that it becomes increasingly pronounced with lower oxidation states.

Further details on the theoretical treatment of the strongly coupled electron-neutral system are included in a separate study, in which we include spectra measured with a wide range of photon energies, which demonstrate unambiguously that this effect is not due to a common coincidence of autodetaching anion states at 2.33 eV above the ground state of the anion.[98]

D. Reliability of the computational results

In most cases, the computational results are in qualitatively good agreement with the experimental results. In previous studies on Ln–O diatomic molecules and a wide range of homometallic cerium oxide clusters, the agreement was generally better than in the current study. We note here that much higher level calculations (spin-orbit complete active space calculations with corrections from second order perturbation theory) on the much smaller SmO^-/SmO molecule recently reported by Neumark and co-workers[75] were in very good agreement with the low-lying electronic structure of SmO; however, those theoretical results did not shed light on the nature of apparently important[99] excited neutral states lying ∼2 eV above the SmO ground state. The more complex systems presented in this current study underscore the distinct challenge this class of systems presents electronic structure calculations. In particular, it appears that a more computationally robust treatment of these complicated electronic states must be developed and an explicit treatment of electron dynamics is necessary to capture essential elements of photodetachment in many lanthanide oxides, especially those including Sm. Efforts of this sort are currently underway in our labs.

V. CONCLUSIONS

A systematic study of small homo- and heteronuclear $Sm_xCe_{3-x}O_y^-$ (x = 0–3; y = 2–4) suboxide molecules using anion PE spectroscopy, supported by a qualitative interpretation of the results of DFT calculations, suggests that small heterometallic Sm-Ce oxides have unique, composition-dependent electronic properties. The spectra compared with computational results suggest interesting x and y-dependent Sm 4f subshell occupancy with implications for Sm-doped ionic conductivity of ceria, as well as the overall electronic structure of the heterometallic oxides. In particular, the Sm centers in the heterometallic species have higher 4f subshell occupancy than the homonuclear $Sm_3O_y^-$/Sm_3O_y clusters. The higher 4f subshell occupancy both weakens Sm–O bonds and destabilizes the 4f subshell relative to the predominantly O 2p bonding orbitals in the clusters. Parallels between the electronic structures of these confined cluster systems with bulk oxides are explored.

In addition, we observe unusual increases in the relative excited state transition intensities in the spectra of $Sm_xCe_{3-x}O_y^-$ (x = 1–3; y = 2, 4) measured with lower photon energies similar to those observed previously in the PE spectra of Sm_2O^- and $Sm_2O_2^-$, suggesting that the phenomenon may be general for species with exceptionally complex electronic structures. The new results suggest that the effect is enhanced with lower oxidation states and more Sm atoms, implying both the prevalence of electrons in the diffuse Sm 6s-based molecular orbitals and a more populated 4f subshell contribute to this phenomenon. Finally, we consider the utility, challenges, and limitations of inexpensive DFT calculations in treating exceptionally complex electronic structures.

SUPPLEMENTARY MATERIAL

See supplementary material for details on spectroscopic parameters used to generate PE spectral simulations, absolute orbital energies from calculations, structures of all species considered in the spectral simulations, diagrams showing all structures and energies that converged in calculations, spin densities, and representative orbitals and occupancies (Cartesian coordinates for all species are available on request) and several direct comparisons of specific species (*vide supra*).

ACKNOWLEDGMENTS

This work was supported by the National Science Foundation Grant No. CHE-1265991. H.P.H. acknowledges support from the Petroleum Research Fund (ACS-PRF No. 56806-DNI6) and the Hellman Fellows Fund for a faculty fellowship. V.M.C. was supported by the National Science Foundation REU Program at IU Chemistry (Grant No. CHE-1460720). S.S.I. acknowledges support from NSF Grant No. CHE-1665336. C.C.J., S.S.I., and H.P.H. gratefully acknowledge additional support for the multi-institutional collaboration from the IU-MSI STEM Initiative, with funding from the Department of Navy Grant No. N000141512423.

[1] S. C. Atkinson, "Crystal structures and phase transitions in the rare earth oxides," Ph.D. thesis, University of Salford, Salford, UK, 2013.
[2] A. Kramida, Yu. Ralchenko, J. Reader, and NIST ASD Team, NIST Atomic Spectra Database (version 5.3) [Online]. Available: http://physics.nist.gov/asd (last accessed March 25 2016), National Institute of Standards and Technology, Gaithersburg, MD, 2015.
[3] J. L. F. Da Silva, M. V. Ganduglia-Pirovano, J. Sauer, V. Bayer, and G. Kresse, Phys. Rev. B **75**, 045121 (2007).
[4] D. R. Mullins, Surf. Sci. Rep. **70**, 42 (2015).
[5] R. J. Gorte, AIChE J. **56**, 1126 (2010).
[6] A. Bruix, J. A. Rodriguez, P. J. Ramírez, S. D. Senanayake, J. Evans, J. B. Park, D. Stacchiola, P. Liu, J. Hrbek, and F. Illas, J. Am. Chem. Soc. **134**, 8968 (2012).
[7] E. S. Bickford, S. Velu, and C. Song, Prepr. Pap.-Am. Chem. Soc., Div. Fuel Chem. **48**, 810 (2003).
[8] T. Bunluesin, R. J. Gorte, and G. W. Graham, Appl. Catal., B **15**, 107 (1998).
[9] A. Luengnaruemitchai, S. Osuwan, and E. Gulari, Catal. Commun. **4**, 215 (2003).
[10] Y. Li, Q. Fu, and M. Flytzani-Stephanopoulos, Appl. Catal., B **27**, 179 (2000).
[11] J. Vecchietti, A. Bonivardi, W. Xu, D. Stacchiola, J. J. Delgado, M. Calatayud, and S. E. Collins, ACS Catal. **4**, 2088 (2014).
[12] S. Hui, J. Roller, S. Yick, X. Zhang, C. Decès-Petit, Y. Xie, R. Maric, and D. Ghosh, J. Power Sources **172**, 493 (2007).
[13] H. Inaba and H. Tagawa, Solid State Ionics **83**, 1 (1996).
[14] F. Y. Wang, S. Chen, and S. Cheng, Electrochem. Commun. **6**, 743 (2004).
[15] S. Zha, C. Xia, and G. Meng, J. Power Sources **115**, 44 (2003).
[16] J. Huang, L. Yang, R. Gao, Z. Mao, and C. Wang, Electrochem. Commun. **8**, 785 (2006).
[17] M. Nolan, J. E. Fearon, and G. W. Watson, Solid State Ionics **177**, 3069 (2006).

[18]F. Yuan, Y. Zhang, and W. J. Weber, J. Phys. Chem. C **119**, 13153 (2015).
[19]T. S. Oh and S. M. Haile, Phys. Chem. Chem. Phys. **17**, 13501 (2015).
[20]D. R. Ou, T. Mori, F. Ye, T. Kobayashi, J. Zou, G. Auchterlonie, and D. Drennan, Appl. Phys. Lett. **89**, 171911 (2006).
[21]A. Tschöpe, J. Y. Ying, and H. L. Tuller, Sens. Actuators, B **31**, 111 (1996).
[22]A. N. Chen, S. B. Adler, and J. Li, Appl. Phys. Lett. **105**, 201602 (2014).
[23]K. Eguchi, T. Setoguchi, T. Inoue, and H. Arai, Solid State Ionics **52**, 165 (1992).
[24]S. M. Haile, Acta Mater. **51**, 5981 (2003).
[25]S. Kuharuangrong, J. Power Sources **171**, 506 (2007).
[26]G. B. Balazs and R. S. Glass, Solid State Ionics **76**, 155 (1995).
[27]W. Huang, P. Shuk, and M. Greenblatt, Solid State Ionics **100**, 23 (1997).
[28]H. Yahiro, Y. Eguchi, K. Eguchi, and H. Arai, J. Appl. Electrochem. **18**, 527 (1988).
[29]T. Kudo and H. Obayashi, J. Electrochem. Soc. **123**, 415 (1976).
[30]H. L. Tuller and A. S. Nowick, J. Electrochem. Soc. **122**, 255 (1975).
[31]J. W. Fergus, J. Power Sources **162**, 30 (2006).
[32]V. V. Kharton, F. M. B. Marques, and A. Atkinson, Solid State Ionics **174**, 135 (2004).
[33]S. M. Lang and T. M. Bernhardt, Phys. Chem. Chem. Phys. **14**, 9255 (2012).
[34]J. E. Mann, N. J. Mayhall, and C. C. Jarrold, Chem. Phys. Lett. **525-526**, 1 (2012).
[35]Y. Suchorski, R. Wrobel, S. Becker, and H. Weiss, J. Phys. Chem. C **112**, 20012 (2008).
[36]F. Yang, J. Graciani, J. Evans, P. Liu, J. Hrbek, J. F. Sanz, and J. A. Rodriguez, J. Am. Chem. Soc. **133**, 3444 (2011).
[37]S. D. Senanayake, P. J. Ramírez, I. Waluyo, S. Kundu, K. Mudiyanselage, Z. Liu, Z. Liu, S. Axnanda, D. J. Stacchiola, J. Evans, and J. A. Rodriguez, J. Phys. Chem. C **120**, 1778 (2016).
[38]Z. Liu, D. C. Grinter, P. G. Lustemberg, T.-D. Nguyen-Phan, Y. Zhou, S. Luo, I. Waluyo, E. J. Crumlin, D. J. Stacchiola, J. Zhou, J. Carrasco, H. F. Busnengo, M. V. Ganduglia-Pirovano, S. D. Senanayake, and J. A. Rodriguez, Angew. Chem., Int. Ed. **55**, 7455 (2016).
[39]P. G. Lustemberg, P. J. Ramírez, Z. Liu, R. A. Gutiérrez, D. G. Grinter, J. Carrasco, S. D. Senanayake, J. A. Rodriguez, and M. V. Ganduglia-Pirovano, ACS Catal. **6**, 8184 (2016).
[40]J. A. Rodriguez, D. C. Grinter, Z. Liu, R. M. Palomino, and S. D. Senanayake, Chem. Soc. Rev. **46**, 1824 (2017).
[41]G. Pacchioni, Phys. Chem. Chem. Phys. **15**, 1737 (2013).
[42]J. Paier, C. Penschke, and J. Sauer, Chem. Rev. **113**, 3949 (2013).
[43]J. Carrasco, D. López-Durán, Z. Liu, T. Duchoň, J. Evans, S. D. Senanayake, E. J. Crumlin, V. Matolin, J. A. Rodriguez, and M. V. Ganduglia-Pirovano, Angew. Chem., Int. Ed. **54**, 3917 (2015).
[44]N. J. Mayhall, D. W. Rothgeb, E. Hossain, K. Raghavachari, and C. C. Jarrold, J. Chem. Phys. **130**, 124313 (2009).
[45]J. B. Kim, M. L. Weichman, and D. M. Neumark, J. Chem. Theory Comput. **10**, 5235 (2014).
[46]J. B. Kim, M. L. Weichman, and D. M. Neumark, J. Chem. Phys. **141**, 174307 (2014).
[47]J. B. Kim, M. L. Weichman, and D. M. Neumark, J. Am. Chem. Soc. **136**, 7159 (2014).
[48]G. Meloni, M. J. Ferguson, and D. M. Neumark, Phys. Chem. Chem. Phys. **5**, 4073 (2003).
[49]J. Czekner, G. V. Lopez, and L. S. Wang, J. Chem. Phys. **141**, 244302 (2014).
[50]B. Schaefer, R. Pal, N. S. Khetrapal, M. Amsler, A. Sadeghi, V. Blum, X. C. Zeng, S. Goedecker, and L. S. Wang, ACS Nano **8**, 7413 (2014).
[51]G. V. Lopez, T. Jian, W. L. Li, and L. S. Wang, J. Phys. Chem. A **118**, 5204 (2014).
[52]I. Leon, Z. Yang, and L. S. Wang, J. Chem. Phys. **139**, 194306 (2013).
[53]G. L. Gutsev, C. A. Weatherford, B. R. Ramachandran, L. G. Gutsev, W.-J. Zheng, O. C. Thomas, and K. H. Bowen, J. Chem. Phys. **143**, 044306 (2015).
[54]K. Lang, B. Visser, D. Neuwirth, J. F. Eckhard, U. Boesl, M. Tschurl, K. H. Bowen, and U. Heiz, Int. J. Mass Spectrom. **375**, 9 (2015).
[55]X. Tang, D. Bumueller, A. Lim, J. Schneider, U. Heiz, G. Gantefor, D. H. Fairbrother, and K. H. Bowen, J. Phys. Chem. C **118**, 29278 (2014).
[56]M. Neumaier, M. Olzmann, B. Kiran, K. H. Bowen, B. Eichhorn, S. T. Stokes, A. Buonaugurio, R. Burgert, and H. Schnockel, J. Am. Chem. Soc. **136**, 3607 (2014).
[57]K. Hirsch, V. Zamudio-Bayer, A. Langenberg, M. Vogel, J. Rittmann, S. Forin, T. Möller, B. von Issendorff, and J. T. Lau, J. Phys. Chem. C **119**, 11184 (2015).
[58]A. Aguado, A. Vega, A. Lebon, and B. von Issendorff, Angew. Chem., Int. Ed. **54**, 2111 (2015).
[59]K. Hirsch, V. Zamudio-Bayer, A. Langenberg, M. Niemeyer, B. Langbehn, T. Moller, A. Terasaki, B. von Issendorff, and J. T. Lau, Phys. Rev. Lett. **114**, 087202 (2015).
[60]L. Ma, B. von Issendorff, and A. Aguado, J. Chem. Phys. **132**, 104303 (2010).
[61]T. Ichino, A. J. Gianola, D. H. Andrews, and W. C. Lineberger, J. Phys. Chem. A **108**, 11307 (2004).
[62]M. Walter, H. Hakkinene, J. Stanzel, M. Neeb, and W. Eberhardt, Phys. Rev. B **76**, 155422 (2007).
[63]N. Pontius, G. Luttgens, P. S. Bechtold, M. Neeb, and W. Eberhardt, J. Chem. Phys. **115**, 10479 (2001).
[64]A. Pramann, K. Koyasu, A. Nakajima, and K. Kaya, Int. J. Mass Spectrom. **229**, 77 (2003).
[65]A. Pramann, Y. Nakamura, A. Nakajima, and K. Kaya, J. Phys. Chem. A **105**, 7534 (2001).
[66]A. Pramann, K. Koyasu, A. Nakajima, and K. Kaya, J. Phys. Chem. A **106**, 4891 (2002).
[67]P. W. Villalta and D. G. Leopold, J. Chem. Phys. **130**, 024303 (2009).
[68]S. R. Miller, N. E. Schultz, D. G. Truhlar, and D. G. Leopold, J. Chem. Phys. **130**, 024304 (2009).
[69]G. Wrigge, M. A. Hoffmann, B. von Issendorff, and H. Haberland, Eur. Phys. J. D **24**, 23 (2003).
[70]R. Klingeler, G. Lüttgens, N. Pontius, R. Rochow, P. S. Bechtold, M. Neeb, and W. Eberhardt, Eur. Phys. J. D **9**, 263 (1999).
[71]R. W. Field, Ber. Bunsenges. Phys. Chem. **86**, 771 (1982).
[72]M. Ray, J. Felton, J. O. Kafader, J. Topolski, and C. C. Jarrold, J. Chem. Phys. **142**, 064305 (2015).
[73]J. O. Kafader, J. E. Topolski, and C. C. Jarrold, J. Chem. Phys. **145**, 154306 (2016).
[74]J. O. Kafader, J. E. Topolski, V. Marrero-Colon, S. Iyengar, and C. C. Jarrold, J. Chem. Phys. **146**, 194310 (2017).
[75]M. L. Weichman, B. Vlaisavljevich, J. A. DeVine, N. S. Shuman, S. G. Ard, T. Shiozaki, D. M. Neumark, and A. A. Viggiano, J. Chem. Phys. **147**, 234311 (2017).
[76]V. D. Moravec and C. C. Jarrold, J. Chem. Phys. **108**, 1804 (1998).
[77]S. E. Waller, J. E. Mann, and C. C. Jarrold, J. Phys. Chem. A **117**, 1765 (2013).
[78]M. J. Frisch, G. W. Trucks, H. B. Schlegel, G. E. Scuseria, M. A. Robb, J. R. Cheeseman, G. Scalmani, V. Barone, B. Mennucci, G. A. Petersson, H. Nakatsuji, M. Caricato, X. Li, H. P. Hratchian, A. F. Izmaylov, J. Bloino, G. Zheng, J. L. Sonnenberg, M. Hada, M. Ehara, K. Toyota, R. Fukuda, J. Hasegawa, M. Ishida, T. Nakajima, Y. Honda, O. Kitao, H. Nakai, T. Vreven, J. A. Montgomery,Jr., J. E. Peralta, F. Ogliaro, M. J. Bearpark, J. Heyd, E. N. Brothers, K. N. Kudin, V. N. Staroverov, R. Kobayashi, J. Normand, K. Raghavachari, A. P. Rendell, J. C. Burant, S. S. Iyengar, J. Tomasi, M. Cossi, N. Rega, N. J. Millam, M. Klene, J. E. Knox, J. B. Cross, V. Bakken, C. Adamo, J. Jaramillo, R. Gomperts, R. E. Stratmann, O. Yazyev, A. J. Austin, R. Cammi, C. Pomelli, J. W. Ochterski, R. L. Martin, K. Morokuma, V. G. Zakrzewski, G. A. Voth, P. Salvador, J. J. Dannenberg, S. Dapprich, A. D. Daniels, Ö. Farkas, J. B. Foresman, J. V. Ortiz, J. Cioslowski, and D. J. Fox, gaussian 09, Revision D.01, Gaussian, Inc., Wallingford, CT, USA, 2009.
[79]X. Cao and M. Dolg, J. Chem. Phys. **115**, 7348 (2001).
[80]R. N. Schaugaard, J. E. Topolski, M. Ray, K. Raghavachari, and C. C. Jarrold, J. Chem. Phys. **148**, 054308 (2018).
[81]J. O. Kafader, M. Ray, K. Raghavachari, and C. C. Jarrold, J. Chem. Phys. **144**, 074307 (2016).
[82]E. P. Wigner, Phys. Rev. **73**, 1002 (1948).
[83]J. Luzon, K. Bernot, I. J. Hewitt, C. E. Anson, A. K. Powell, and R. Sessoli, Phys. Rev. Lett. **100**, 247205 (2008).
[84]A. M. Burrow, T. Wende, M. Sierka, R. Wlodarczyk, J. Sauer, P. Claes, L. Jiang, G. Meijer, P. Lievens, and K. R. Asmis, Phys. Chem. Chem. Phys. **13**, 19393–19400 (2011).
[85]B. L. Yoder, J. T. Maze, K. Raghavahcari, and C. C. Jarrold, J. Chem. Phys. **122**, 094313 (2005).
[86]P. J. Robinson, X. Zhang, T. McQueen, K. H. Bowen, and A. N. Alexandrova, J. Phys. Chem. A **121**, 1849 (2017).
[87]H. B. Lal and K. Gaur, J. Mater. Sci. **23**, 919 (1988).
[88]E. van der Kolk and P. Dorenbos, Chem. Matter **18**, 3458 (2006).

[89]J. O. Kafader, M. Ray, and C. C. Jarrold, J. Chem. Phys. **143**, 034305 (2015).
[90]H. Harb, L. M. Thompson, and H. P. Hratchian, "An electronic structure theory study of the photoelectron spectra of EuO^-, EuH^-, and $EuOH^-$" (to be published).
[91]J. A. Felton, M. Ray, and C. C. Jarrold, Phys. Rev. A **89**, 033047 (2014).
[92] "Bond dissociation energies," in *CRC Handbook of Chemistry and Physics*, 98th ed., edited by J. R. Rumble (CRC Press/Taylor & Francis, Boca Raton, FL, 2018), Internet Version.
[93]K. P. Kepp, Inorg. Chem. **55**, 9461 (2016).
[94]P. J. Hay, R. L. Martin, J. Uddin, and G. E. Scuseria, J. Chem. Phys. **125**, 034712 (2006).
[95]K. T. Jacob and A. Rajput, J. Chem. Eng. Data **61**, 1710 (2016).
[96]K. T. Jacob, A. Dixit, and A. Rajput, Bull. Mater. Sci. **39**, 603 (2016).
[97]J. N. Beukers, J. E. Kleibeuker, G. Koster, D. H. A. Blank, G. Rijnders, H. Hilgenkamp, and A. Brinkman, Thin Solid Films **518**, 5173 (2010).
[98]J. L. Mason, J. E. Topolski, S. S. Iyengar, and C. C. Jarrold, "Photoelectrons are not always quite free" (to be published).
[99]P. A. Bernhardt, C. L. Siefring, S. J. Briczinski, A. Viggiano, R. G. Caton, T. R. Pedersen, J. M. Holmes, S. Ard, N. Shuman, and K. M. Groves, Radio Sci. **52**, 559 (2017).